

RADCAM - A Radiation Camera System Combining Foil Bolometers, AXUV Diodes and Filtered Soft X-Ray Diodes

U. A. Sheikh¹, L. Simons¹, B. P. Duval¹, O. Février¹,
D. Moret¹, A. Allegrucci¹, M. Bernert², F. Crisinel¹,
T. Tersztyánszky¹, O. Villinger¹

¹ École Polytechnique Fédérale de Lausanne (EPFL), Swiss Plasma Center
(SPC), CH-1015 Lausanne, Switzerland

² Max Planck Institute für Plasmaphysik, Boltzmannstr. 2, 85748 Garching,
Germany

The author to whom correspondence may be addressed: umar.sheikh@epfl.ch

September 2022

Abstract.

Measurements of radiated power are critical for characterising and optimising tokamak performance. The RADCAM system, comprising arrays of foil bolometers, Absolute eXtreme UltraViolet (AXUV) and filtered soft X-ray diodes, has been constructed to provide improved measurements of plasma radiation on “Tokamak a Configuration Variable” (TCV). An overview of the physical geometry, electronics and design of the system is provided. The construction of the bolometer foils together with the improved sensitivity characteristics resulting from the inclusion of an anti-reflection carbon coating are presented. The large number of lines of sight in RADCAM are shown to significantly increase the spatial resolution over the legacy system. The system calibration procedure is detailed and the mean system sensitivity is shown to vary by less than 5% over 1000 discharges. Additionally, the methodology for cross-calibration of the AXUV diodes with the bolometer foils is presented and applied to generate high temporal resolution measurements. The RADCAM radiation camera system is a compact, versatile system that is demonstrated to provide high resolution profiles of the radiated power in TCV.

Keywords: Bolometers, AXUV diodes, tomographic inversions

1. Introduction

An accurate power balance in a tokamak is critical for all experiments. In certain scenarios, such as those focussed on divertor physics or disruption mitigation, radiated power can account for the bulk of total energy exhaust [1, 2, 3, 4]. Foil bolometers have traditionally been used on tokamaks to measure radiated power as they can be absolutely calibrated in-situ and without a radiation source. These bolometers traditionally consist of thin gold or platinum foils to withstand the nuclear environment [5, 6, 7]. The shortcoming of such foils is the relatively slow temporal resolution due to high thermal mass, resulting in ms range resolution in normal operation and making their use challenging in fast events such as disruptions or Edge Localised Modes (ELMs).

Diode based detectors such as the Absolute eXtreme UltraViolet (AXUV) have been employed on a number of tokamaks to infer total radiated powers at temporal resolution down to a μs [8, 9, 10, 11, 12, 13, 14]. The drawback of these diodes is their inability to retain calibration post installation due to strong sensitivity degradation in the crucial ultraviolet (UV) range [11]. Studies on the ASDEX Upgrade tokamak indicate that the sensitivity of the AXUV diodes in the UV spectral range begins to degrade almost immediately following exposure to tokamak radiation [11].

The RADCAM system on “Tokamak a Configuration Variable” (TCV) was motivated by a need to reduce uncertainty in radiated power measurements, increase the spatial resolution of radiation emission and to provide absolute measurements of radiated power during fast events [15]. To achieve this, the legacy bolometry, AXUV diode and soft X-ray (SXR) tomographic systems were replaced with a single system that integrated all three types of detectors in the same sector [16, 17, 18]. Overlapping lines of sight within this novel system enable cross calibration between the bolometers and diodes, providing radiated power measurements of fast events that can not be resolved by foil bolometers alone. Furthermore, combining the three systems into a compact camera has liberated 16 precious ports of the TCV vacuum vessel.

2. System Design and New Developments

Combining three systems into one camera module generated significant design challenges such as limited port space availability, obtaining full poloidal coverage for each diagnostic, thermal management of three differing systems and electromagnetic shielding. A modular approach was taken to maintain versatility in the camera design, allowing diodes and foil bolometers to be substituted independently as shown in Figure 1. Electronically grounded and TiO₂/Al₂O₃ coated baffles were installed to provide light and electronic noise shielding and reduce reflections within the camera. These design aspects of the system are detailed in the following subsections.

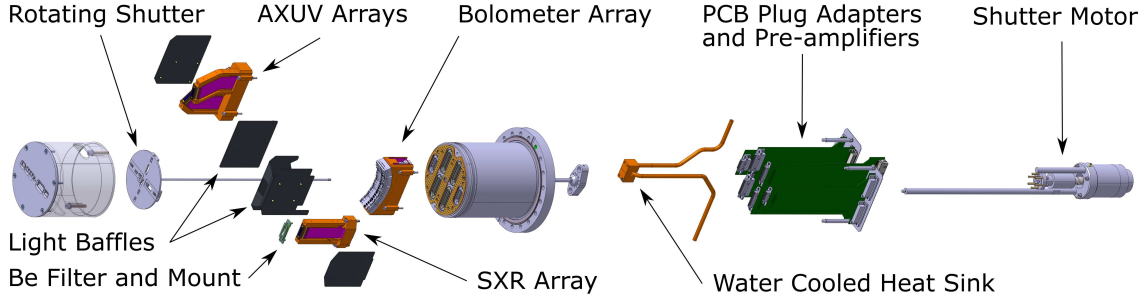


Figure 1. Exploded view of the upper lateral camera with 20 bolometers, 40 AXUV diodes (2 arrays) and 20 SXR filtered diodes.

2.1. Lines of Sight

The total number of lines of sight (LOS) were 120, 140 and 80 for the bolometry, AXUV and SXR systems respectively and are shown in Figure 2. The highest radiation emission region with the strongest emission gradients is typically the divertor, which is at the bottom of the vessel in standard operation. As the divertor is colder than the plasma core, the emitted photon energies are typically in hundreds of eV or less. Thus, the lower lateral (divertor) camera was equipped with a second foil bolometer array and AXUV diodes in the place of SXR filtered diodes as significant SXR emission is less prevalent there. The mid lateral camera was equipped with two SXR filtered diodes arrays to increase core plasma resolution and facilitate mapping of rotating core magnetohydrodynamic (MHD) modes. A second AXUV

module in the upper lateral camera provides increased spatial coverage for disruption experiments engendered by massive gas injection through an upper lateral port in the adjacent sector. Finally in the list of initial configuration choices, the vertical cameras were made symmetric with the SXR filtered diodes placed further from the entrance slit to provide higher spatial resolution of the plasma core. It should be noted that this configuration is optimised for the current baffled configuration, which can be altered between campaigns [19]. Thus, the modularity of the cameras allows sets of LOS to be changed between campaigns if desired.

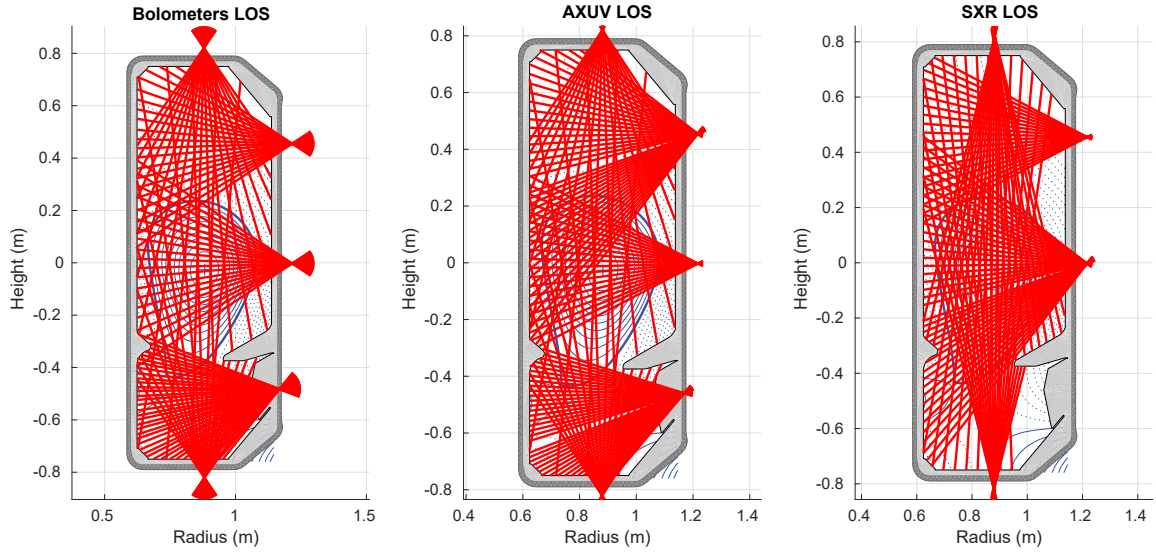


Figure 2. Lines of sight for the foil bolometers (left), AXUV diode (center) and SXR filtered diode (right) systems.

The LOS spacing was optimized to ensure maximum poloidal coverage and only partial overlap between adjacent channels. Physical factors, such as potential heat flux on the front end of the cameras, limited the proximity of the apertures to the plasma. The apertures in the divertor could be placed relatively closer to the plasma due to the presence of protection tiles (shown at a height of -0.5 m in Figure 2). The distance between the detectors and apertures was set to ensure that all poloidal locations were observed by a whole detector or overlapping adjacent detectors with partial detector illumination. Details regarding the viewing cones are provided in Appendix 7.1.

2.1.1. Bolometer System Design Resolution Analysis

A phantom analysis was performed to estimate the increase in resolution of topographically inverted images with the new design. A SOLPS ITER [20] simulation of a common TCV discharge was used to generate an emission profile and synthetic bolometer foil signals. A simplified model without noise or systematic error was applied to generate the synthetic bolometer foil signals. The signals were then tomographically inverted using the standard inversion code at TCV [21] and compared to the original profiles, Figure 3. A false zero in the color scale is used to make the differences more apparent and further details on the tomographic inversions are provided in Appendix 7.2.

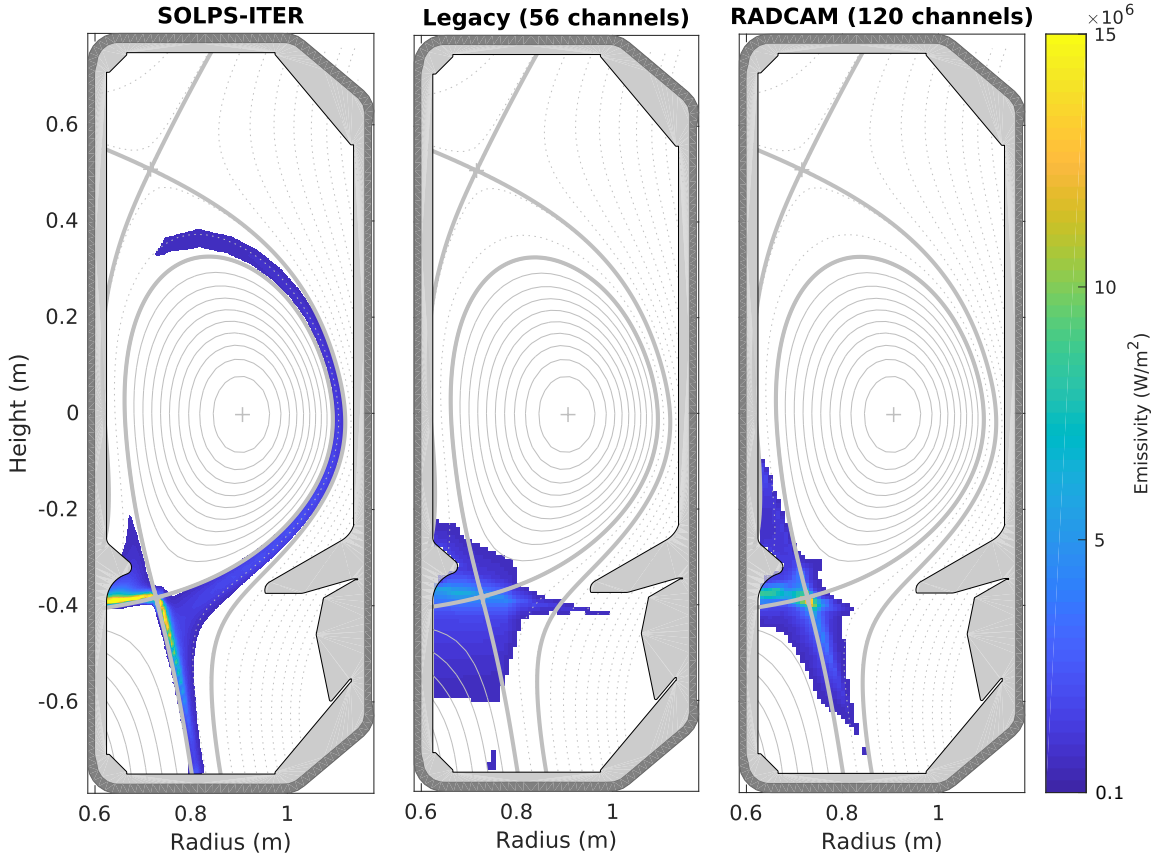


Figure 3. Comparison of tomographically inverted images produced with the legacy (middle) and RADCAM (right) bolometry systems using a simulated phantom from SOLPS-ITER(left).

Neither system was able to resolve the low radiation emission at the edge of the core plasma and this is attributed to the high difficulty in resolving such a narrow and low emission region. Conversely, The increased number of bolometer foils in the RADCAM design significantly increase the reconstructed spatial resolution around the x-point and down the divertor leg. Furthermore, inversion artefacts such as LOS-streaks and emission at the bottom of the inner wall are strongly reduced by the higher resolution RADCAM system as it is able to better constrain the inversion.

2.2. Camera Assembly and Electronics

Connecting a large number of detector channels in a restricted space and within a high vacuum environment required novel solutions. For optimum space utilization, the detector mounting modules were machined from copper to increase thermal conductivity and electromagnetic shielding. The high number of electrical signals were carried by electromagnetically shielded flexible Printed Circuit Boards (PCB), known as “flex PCBs”, that were installed within the copper mounting modules. An example of an AXUV diode mounting assembly is shown in Figure 4.

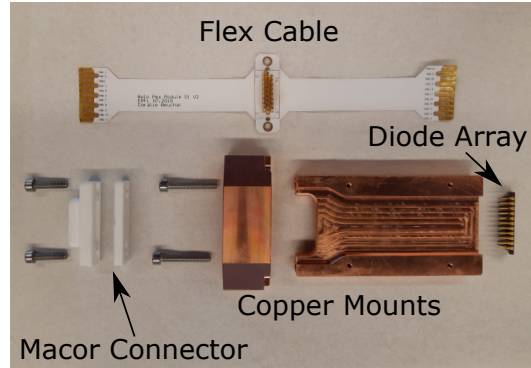


Figure 4. Assembly of an AXUV diode array on a copper module with a printed flex PCB.

The flex PCBs comprised of four copper layers with insulating Kapton layers between each of them, as shown in Figure 5. The two outer copper layers consisted of an electromagnetic noise shielding square grid with an aperture size of 0.5 mm and copper strip width of 0.2 mm. A grid of this size was found to be sufficient to insulate electromagnetic noise at frequencies of upto 50 kHz. The inner two layers

contained the current carrying channels (red lines in Figure 5) surrounded by the electromagnetic shielding grid. The wires were horizontally offset in the adjacent vertical layers to increase the distance between wires, leading to a reduction in cross-talk and an increase the electromagnetic shielding. Kapton was used as the electrically insulating material due to its vacuum compatibility.

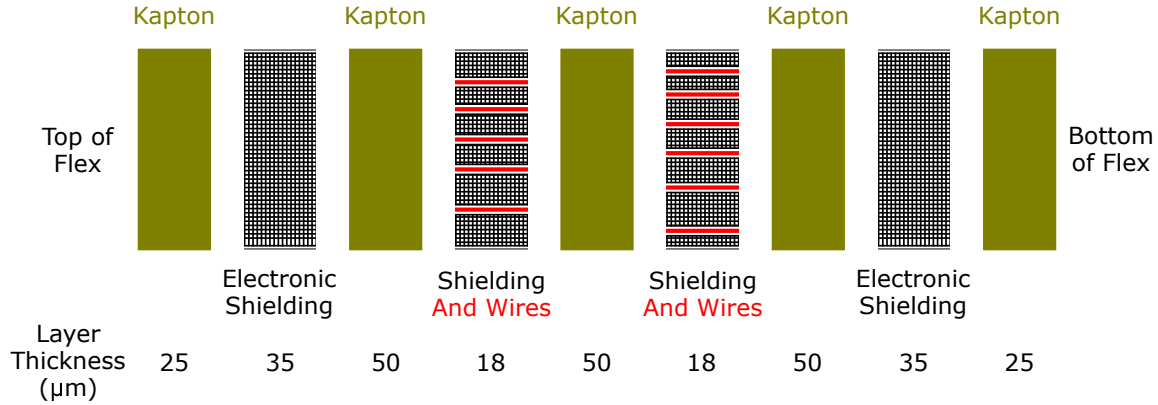


Figure 5. Layered construction of the flex PCB. Signal carrying wires shown in red.

Connections between the flex PCBs and the detectors were made by securing pins into polyether ether ketone (PEEK) connectors. The connectors were used to maintain pin spacing and facilitate detector mounting. An example schematic of the bolometer mounting assembly is shown in Figure 6. Specifically for the bolometers, an additional PEEK insulating piece, indicated in blue in Figure 6 right, was installed between the bolometer heads and the flex connectors to prevent short circuits through the metal body of the bolometers. The diode systems did not require this additional insulator as their housing is non-conducting.

Vacuum compatible, high pin density sub-D connectors made of Macor were used at the vacuum interface. This required precision soldering of the pins directly onto the flex PCB, as shown in Figure 7. The soldering was done manually and with lead free solder to reduce out-gassing. The Macor connectors were then mounted using screws which utilised through holes on the flex PCBs. Slots were cut into the screws to prevent trapping of gases, which would reduce pumping efficiency within the tokamak. The assembly was tested in a high vacuum chamber to ensure acceptable out-gassing rates and tokamak vacuum compatibility.

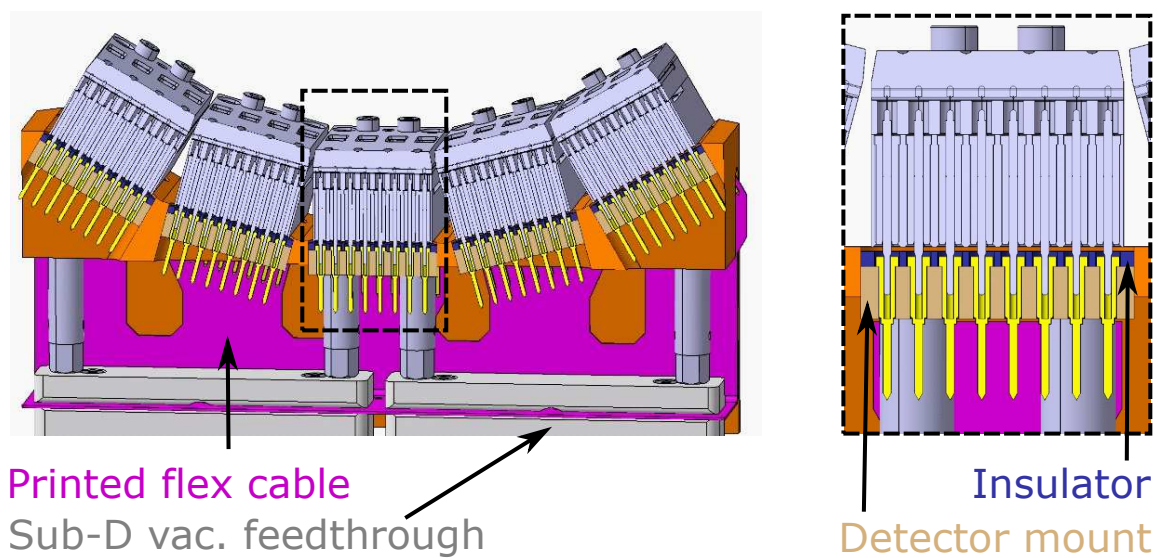


Figure 6. Cut away of a bolometer module assembly (left). Zoomed in image of a single bolometer head with the pin mounting scheme and insulator indicated (right).

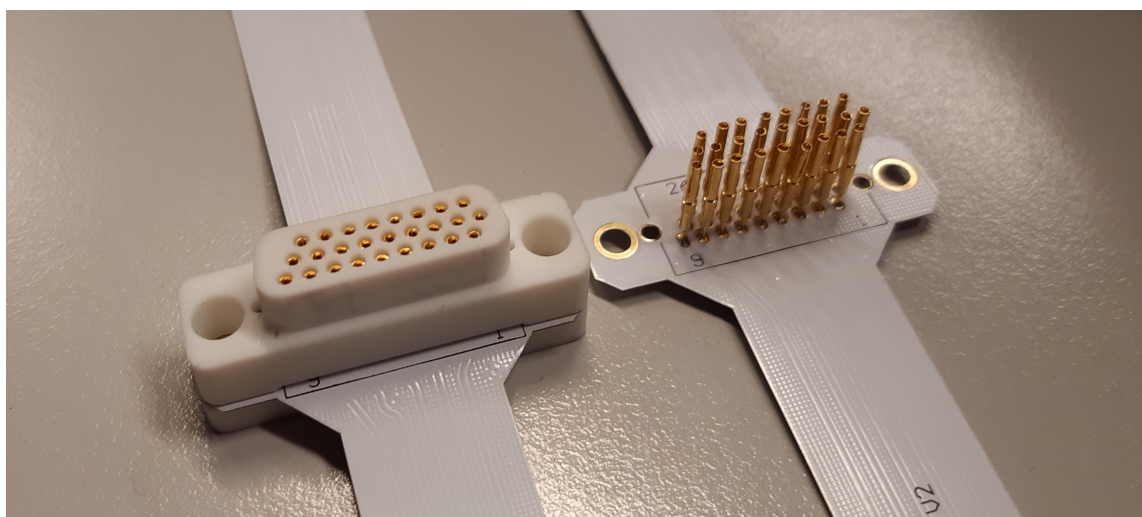


Figure 7. Macor mounting assembly onto a flex PCB. Left - mounted connector. Right - Connector pins soldered directly onto a flex PCB.

Printed PCB cards on the atmospheric side of the cameras provided amplification for the diode systems and the interface to category 7 Ethernet cables for the bolometers. These PCB cards included a shielding layer either side of the printed circuit to increase shielding into the twisted pair transmission lines. The diode amplifiers included both gain, transimpedance and a low pass filter of -3 dB at 105 kHz. This gain is configurable to adapt to the dynamic range of the incoming signal and optimise noise control. The amplifier circuit used is presented in Figure 8. The gain for each camera was selected through empirical testing of the signal level obtained. The gains, normalized to the top vertical camera, are given in Table 1. Absolute gains are not provided as the equivalent resistance of the diode is unknown. Furthermore, calibration with a source was not done as the response of the diodes has been shown to degrade over time and a cross-calibration with the bolometers was planned (described in Section 4.2) [11].

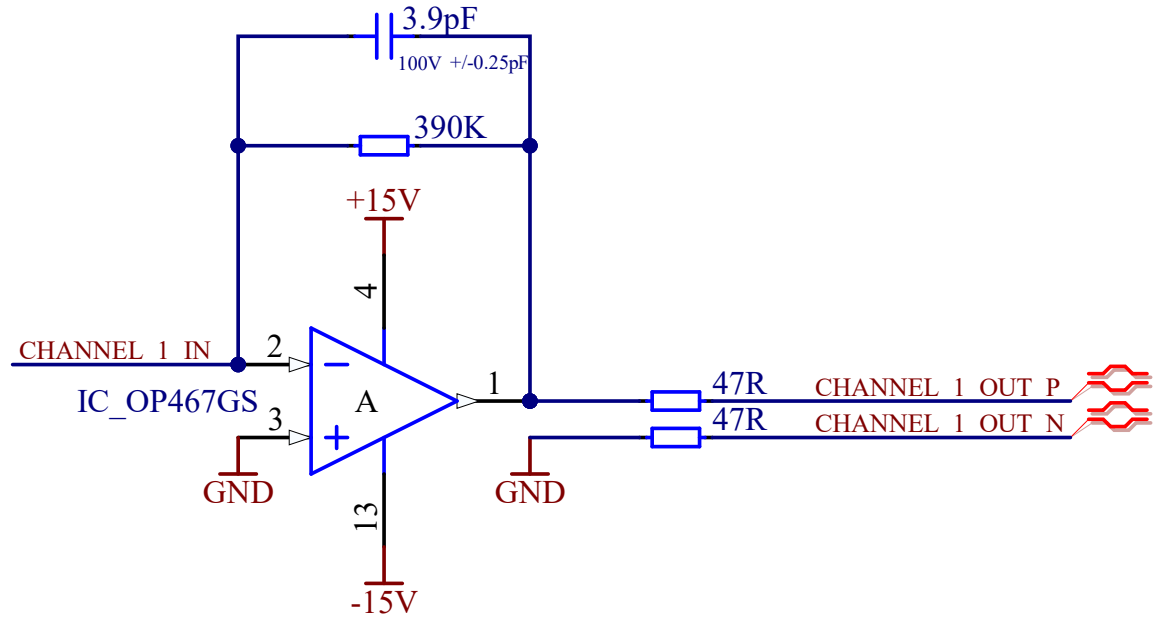


Figure 8. Circuit diagram of the operational amplifier used to amplify the diode signal.

| Camera | AXUV | SXR |
|-----------------|------|-----|
| Vertical Top | 1.0 | 1.0 |
| Upper-Lateral | 2.2 | 0.8 |
| Mid-Lateral | 2.2 | 0.8 |
| Divertor | 3.9 | N/A |
| Vertical Bottom | 1.0 | 1.0 |

Table 1. Gain factors normalised to the top vertical camera for diode systems.

2.3. Thermal Management

The TCV tokamak is baked at up to 230°C after each atmospheric pressure venting cycle requiring a cooling solution to prevent detector damage. This was performed via conduction through the copper mounts to a brazed copper feed-through in the vacuum flange to an ex-vessel, water cooled, heat exchanger. A brazed copper component in the vacuum flange was needed as the low thermal conductivity of the stainless steel flange was insufficient. With the heat exchanger outside of the vacuum vessel, possible water leaks inside the vacuum chamber are avoided. Convective air cooling employing a heat sink was investigated through the program SolidWorks(R). The steady state detector temperatures were estimated using finite element analysis and the results are presented in Figure 9. Air cooling through natural convection alone resulted in detector temperatures of $\sim 130^{\circ}\text{C}$, above the specified tolerance for the diodes. With water cooling of the copper feed-through temperatures of $\sim 50^{\circ}\text{C}$ were obtained and thus it was adopted. Thermocouples were installed on the copper mounts of the cameras to monitor the temperature during baking. A maximum temperature of 45°C was measured on the top vertical camera during baking, indicating the cooling system operates efficiently and ensuring detector temperatures always remain well within manufacturer's tolerances.

2.4. ECRH Protection System

Incident electron cyclotron resonance heating (ECRH) power, even when not specifically directed towards the previous foil bolometers, led to the diagnostic becoming unusable during a discharge and sometimes suffering damage from the heat flux [11]. To counteract this, an inter-discharge selectable protective metal grid was

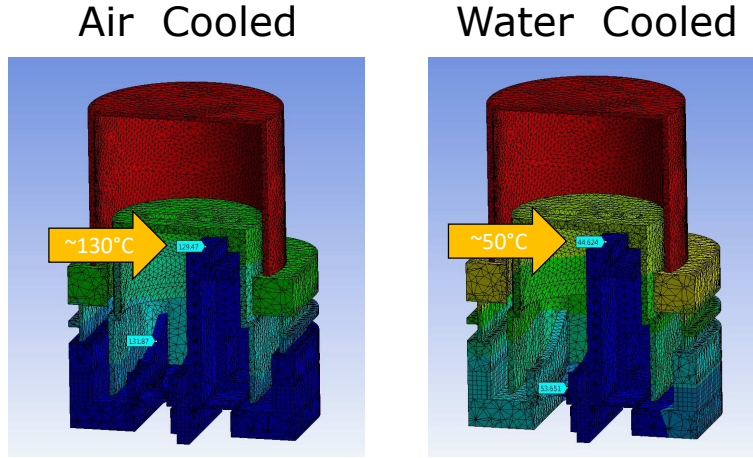


Figure 9. Finite element analysis of detector temperature during TCV bake out for natural convection cooling with a heat sink (left) and water cooling coupled to the copper heat feed-through (right).

installed on a rotating pneumatic motor driven system. Aside from grid placement, the rotating wheel provides protection for the detectors when not in use and a clear aperture when the ECRH protection grid is not required, as shown in Figure 10. The grids were installed with a radius of curvature matching the distance between the detectors and the apertures to maintain the grid approximately perpendicular to the LOS for all channels on a given camera.

The selection of the grid wire thickness and mesh size was based upon minimising ECRH transmission whilst maximising plasma radiation transmission. Three stainless steel rectangular meshes made from wires and two circular grids made from stainless steel (SS) and copper (Cu) sheet were analyzed by their transmission properties whose dimensions are listed in Table 2.

Microwave transmission of each grid was measured using a tunable gyrotron frequency test stand. The gyrotron power was measured by a calorimeter with and without the grid installed. The stand resolution was 0.028 GHz between 80 and 110 GHz and 0.044 GHz between 110 and 120 GHz. The resulting transmission fraction as a function of frequency for each grid is presented in Figure 11 left. The standard X2 and X3 gyrotron frequencies injected into TCV are indicated by the dashed black lines.

The measured transmission ranged from 16% to less than 0.5%. The circular hole



Figure 10. Image of the rotating plate with the grids and apertures of a RADCAM camera module.

Table 2. Dimensions of the grids studied for ECRH protection.

| Grid | Mesh Size | Wire Diameter | Hole Diameter | Inter-hole Spacing |
|--------------------|-----------|---------------|---------------|--------------------|
| Rectangular Mesh 1 | 0.465 mm | 0.125 mm | - | - |
| Rectangular Mesh 2 | 0.315 mm | 0.112 mm | - | - |
| Rectangular Mesh 3 | 0.265 mm | 0.100 mm | - | - |
| SS Circular Grid | - | - | 0.4 mm | 0.5 mm |
| Cu Circular Grid | - | - | 0.4 mm | 0.5 mm |

grids produced better microwave shielding than the rectangular mesh with higher frequencies showing increased transmission for all grids. To assess the corresponding visible light attenuation by the grids, a 2 W, 445 nm laser diode was shone upon three bolometer foils and an average transmission measured that minimised the effects of alignment sensitivity. The measured transmission at 445 nm, geometrical transparency fraction based on the mesh dimensions and transmission at X2 and X3 frequencies are presented in Table 3.

The rectangular mesh grids showed significantly higher visible light transmission than the circular grids. The high attenuation of the circular grids is attributed to their higher solid surface area. Rectangular mesh 3 (the thinnest wire mesh with the smallest grid size) gave the highest attenuation of microwave frequencies whilst

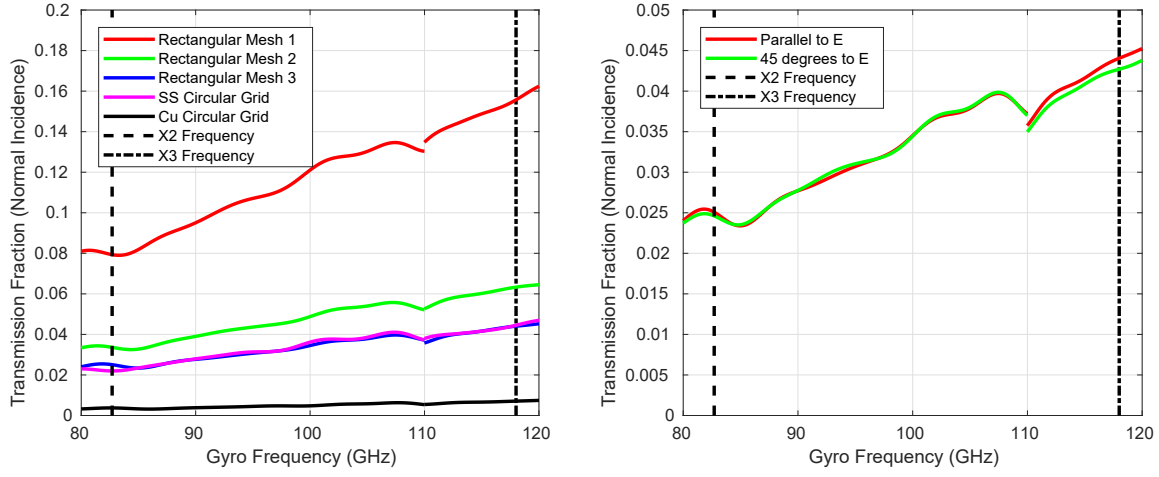


Figure 11. Left - Normal incidence transmission properties of the ECRH protection grids. Right - Influence of grid orientation relative to gyrotron wave angle.

Table 3. Transmission properties of the three rectangular grids and stainless steel (SS) and copper (Cu) circular grids measured using a gyrotron test stand and a 445 nm laser.

| Grid | 82.7 GHz (X2) Transmission | 118.0 GHz (X3) Transmission | 445nm Laser Transmission | Geometrical Transparency Fraction (%) |
|-----------------------|-------------------------------|--------------------------------|-----------------------------|---|
| Rectangular Mesh 1 | 7.9% | 15.6% | 65±5% | 62% |
| Rectangular Mesh 2 | 3.4% | 6.3% | 58±5% | 54% |
| Rectangular Mesh 3 | 2.5% | 4.4% | 56±5% | 53% |
| SS Circular Grid | 2.2% | 4.4% | 47±4% | 50% |
| Cu Circular Grid | 0.4% | 0.7% | 52±4% | 50% |

maintaining 56% transmission of 445 nm light and was selected for use in the cameras. Sensitivity of the grid orientation was found to be negligible by placing the mesh parallel to the electric field (E) and at an angle of 45 deg, Figure 11 right.

The small percentage of ECRH power that is able to traverse the protection grid may still have a detrimental impact on incident radiation measurements. It is highly unlikely that direct power can reach the detectors based on the tokamak geometry and positions of the ECRH launchers. Therefore, it is mainly the reflections within the camera that need to be avoided. It was shown through experiments on the ASDEX Upgrade tokamak that TiO₂/Al₂O₃ coatings on the internal camera components can reduce the stray power measured by the bolometers by over a factor of 3 [22]. The same coating material was also used as an absorber for the water baffle of W7-X cryopumps [23]. Based on these studies, TiO₂/Al₂O₃ coatings were applied to all light and electronic noise shielding structures in the camera assembly.

2.5. Data Acquisition Systems

Two separate data acquisition systems were required for the diode and bolometer style detectors. The diodes simply generate a photo-current that is amplified on the atmospheric side of the camera and conducted to a D-TACQ ACQ196CPCI data acquisition system sampling at 200 kHz [24].

Conversely, the foil bolometers require bridge excitation to increase the sensitivity of the system. To produce this excitation signal and acquire the data, a D-TACQ ACQ400 series system with BOLO8BLF hardware was employed [25]. The bridge was excited by a sine-wave with an amplitude of $9 V_{p-p}$ and a frequency of 18 kHz for the discharges presented in this study. Excitation voltages of up to $18 V_{p-p}$ are possible and will be explored in the future with a view to noise performance and their impact upon component lifetime.

This specialised D-TACQ hardware utilises a Field Programmable Gate Array (FPGA) to control the bolometer excitation signal and pre-treat the recorded signal. This provides flexibility in the excitation programming and the choice of acquired signal, decimation parameters, filtering and generation of real time power measurements. The BOLO8BLF system is also able to provide the Ohmic heating used to calibrate the bolometers outside of TCV discharges, enabling tracking and study of the system.

3. Detectors

3.1. Bolometers

The foil bolometers were produced in collaboration with the Max Planck Institute for Plasma Physics and Fraunhofer Institute for Microtechnology and Microsystems. The design followed that of the ITER foil bolometers with changes to absorber thickness for use on TCV. Specifically, the absorber thickness was reduced to $3\text{ }\mu\text{m}$ to increase bolometric sensitivity by reducing the sensor's thermal mass. Any further reduction in absorber thickness unacceptably increases the transmission of higher energy photons, Figure 12, left. For a $3\text{ }\mu\text{m}$ thickness, gold foil absorbs all photons below an energy of 4 keV . This is sufficient for most TCV operation where plasma emission in the multi-keV energy range is rarely expected to be a large fraction of total emission.

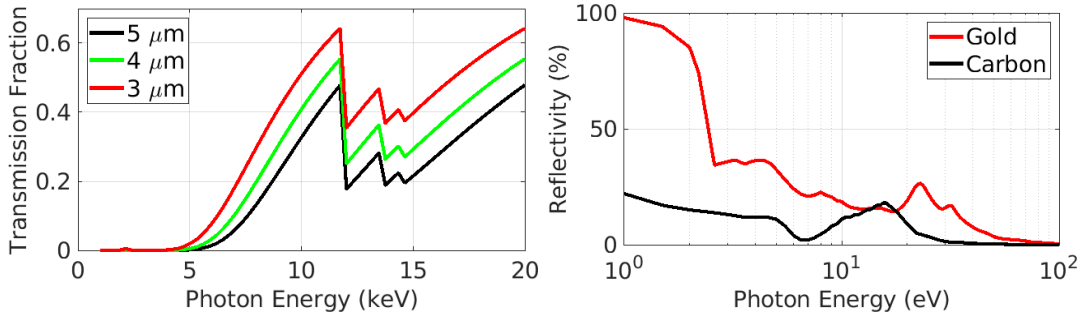


Figure 12. Left - Attenuation of high energy photons by a gold absorber. Right - Reflectivity of gold and carbon layers at 75° angle of incidence with a thickness of 10-60 nm.

The front surface of the gold absorber was coated with 50 nm of carbon to reduce reflections, particularly of UV and visible light, thus providing a more accurate measure of incoming power [26]. Carbon coatings on foils have been utilized previously to reduce reflections and the first quantification of their impact was done on TCV, where up to a 15% increase in radiated power was observed relative to bolometers without the coating [27, 28, 29]. This is predominantly from reduced reflectivity in the 1-100 eV photon range, Figure 12, right. This energy range is of particular importance in TCV due to its focus on divertor studies, where a larger proportion of the radiated power is in the UV/visible part of the spectrum. A coating

thickness of 50 nm was sufficient to reduce the reflections whilst only increasing the thermal mass, and thus reducing the detector sensitivity, by $\sim 5.5\%$.

A 200 nm platinum thermal conduction layer underneath the gold absorbing layer was included to reduce the bolometer cooling time and maintain a lower absorber temperature during experiments[30]. This is beneficial as it maintains a lower bridge imbalance, thus reducing the working voltage range, which can in turn be captured at a higher resolution. Reducing the variation in foil temperature during a discharge also ensures the validity of the calibration done prior to the experiment. The material responses of gold and platinum to environmental changes, such as temperature cycling, are similar and thus delamination is not expected. Temperature cycling tests were conducted to confirm this. Below the thermal conduction layer, chromium-oxide was used as an adhesion promoter between the membrane and platinum based on its stability[31, 32]. The layered construction of the foils is depicted in a simplified form in Figure 13.

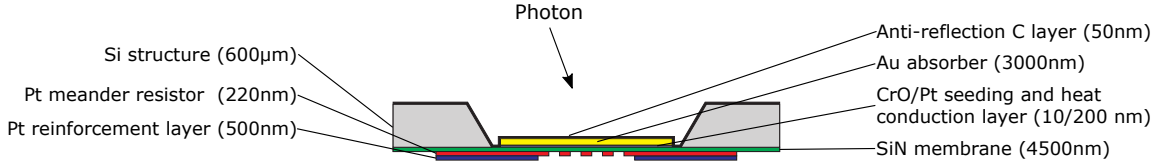


Figure 13. Layered composition of the bolometer foil.

3.2. Diode Systems

The RADCAM uses AXUV20ELG diode arrays from OptoDiode[33]. The arrays consist of 20 diodes, each with a sensitive area of $0.75\text{ mm} \times 4.1\text{ mm}$ and 0.20 mm gaps between active regions. The same diode arrays were used in the AXUV and SXR systems to simplify the design and increase the modularity of the system. No bias voltage was applied to these diodes as the design of the AXUV20ELG diode arrays does not allow it.

3.2.1. SXR Photon Filter Selection

Beryllium foils were selected for the SXR system to absorb photons below $\sim 1\text{ keV}$, to prevent the most common atomic line emission from TCV plasmas reaching the detectors. A foil thickness of $47\text{ }\mu\text{m}$ was selected to balance between line radiation

filtering and obtaining a sufficiently strong SXR signal from the hotter plasma core. Figure 14 plots the foil transmission curve and is overlaid with the photon energies of the highest bound-bound emission lines for the two most common impurities observed on TCV; C (475 eV) from the walls and N (650 eV) injected during high radiation emission experiments.

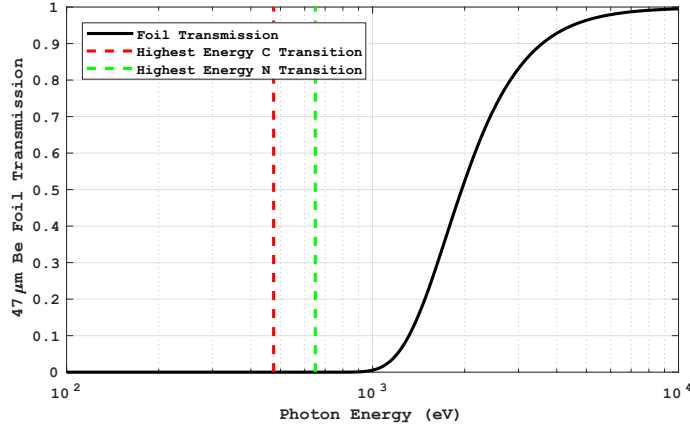


Figure 14. Transmission of a $47\ \mu\text{m}$ Be foil and energies of the highest bound-bound emission lines for N and C. Sources [34, 35].

The filters were mounted flat on to the diodes in the vertical cameras whereas a curved mounting structure was used in the horizontal cameras. The distance between detector and slit in the vertical cameras is 36.3 mm, corresponding to an effective foil thickness at the edge channels of $49\ \mu\text{m}$. The consequent variation in transmission is negligible in the integration of SXR energy. The distance between the detector and slit was 17.5 mm for the horizontal cameras and therefore the effective thickness at the edge of the array increases to over $65\ \mu\text{m}$. This results in a non-negligible variation in SXR filtering, so curved mounting pieces, presented in Figure 15, were installed on the detectors. The radius of curvature was set to match the distance between detector and slit, ensuring an effective filter thickness of $\sim 47\ \mu\text{m}$ for each diode.

4. Data Analysis and System Performance

The RADCAM system has reliably operated on TCV for over 5000 discharges at the time of writing. The legacy bolometry system was still available during the first of

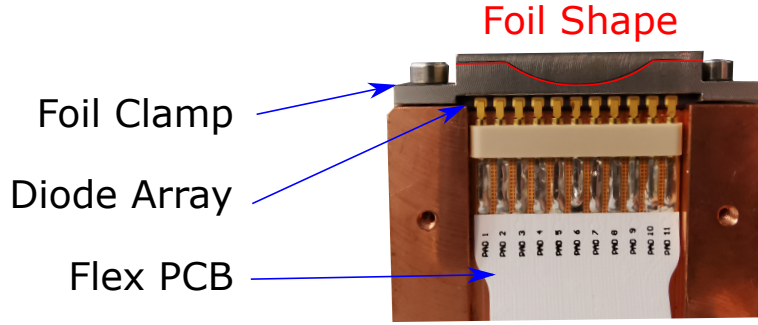


Figure 15. Curved beryllium filter mounting assembly. Foil shape outlined in red.

these 800 discharges and allowed for a comparison between the system. The legacy bolometers did not include a carbon coating on the foils and thus this comparison enables an investigation of its influence upon bolometric measurements.

4.1. Bolometer System Calibration

To obtain absolute incident radiated power measurements, the sensitivities of the foils to a given heating power and their cooling constants are required. These are obtained by measuring the system response to known Ohmic heating and the Wheatstone bridge voltage decay rate once such heating has ceased. Excitation of the bridge is maintained throughout this process to ensure comparable conditions with experimental measurements. For the Ohmic heating phase, a 1.1 V difference is applied across each measurement resistor. The Ohmic heating current, I_{OH} , and voltage, V_{OH} , are measured during this process at the locations indicated in Figure 16.

A total Ohmic heating power, $P_{OH} = 2I_{OH}V_{OH}$, of ~ 2.2 mW is supplied to the measurement resistors by the BOLO8BLF system for 1 s, allowing the system to stabilise, as shown in Figure 17. The sensitivity is then calculated from the ratio of the voltage change across the bridge to the applied Ohmic heating. These values are averaged over ~ 200 ms once the bridge has equilibrated, as indicated by the red dashed lines in Figure 17 left. The cooling coefficient, τ , is computed using an exponential fit to the bridge voltage decay following the heating pulse. The fitting region is represented by the red dashed line in Figure 17 right and the fitted curve is indicated by the superimposed green line. This process is controlled by the FPGA

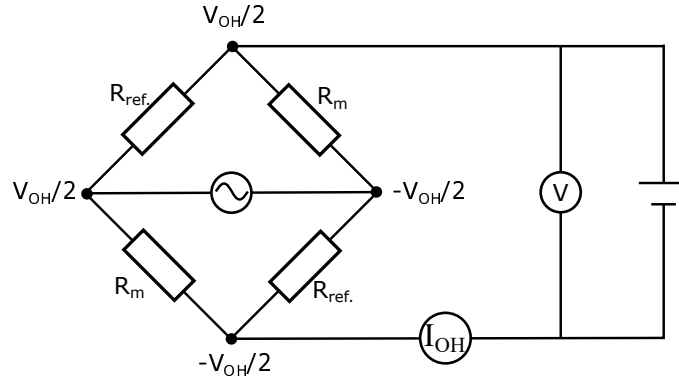


Figure 16. Electronic circuit during calibration depicting the positions of the measurement (R_m) and reference ($R_{ref.}$) resistors, Ohmic heating voltage (V_{OH}) and current (I_{OH}).

system and conducted prior to each plasma pulse, resulting in a calibration that tracks operating conditions.

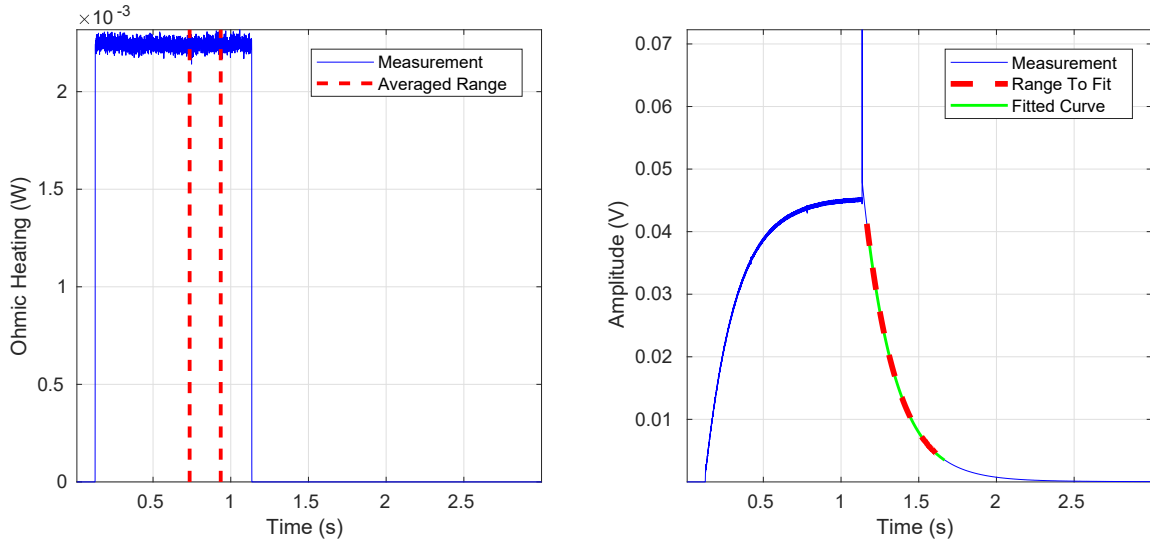


Figure 17. Left - Representative calibration measurement with Ohmic heating of the bridge. Time region averaged to calculate sensitivity indicated by red dashed lines. Right - Measured voltage across the bridge during calibration. Exponential decay region used for fitting indicated by red dashed line and fitted curve superimposed by green line.

An average τ of 0.20 s and sensitivity of 20.8 V/W were measured with a variance of less than 10% across most channels. The sensitivity and cooling time for each foil is presented in Figure 18 with $\pm 10\%$ of the average indicated by dashed black lines. The system sensitivity averaged across all channels varied by less than 2% for the bulk of 1000 calibrations conducted prior to tokamak discharges and details are presented in Appendix 7.3.

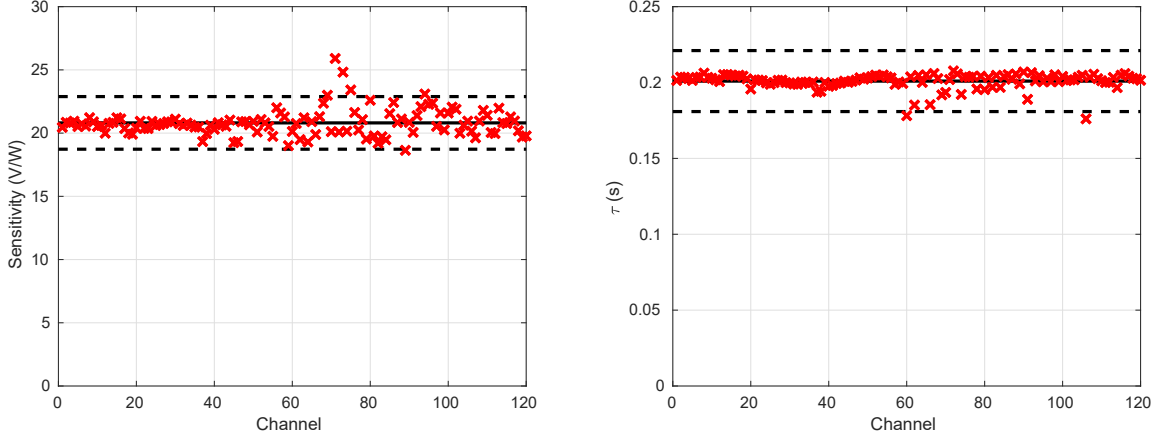


Figure 18. Sensitivities (left) and cooling times (right) of the bolometer foils.

4.2. Sensitivity Calibration of AXUV Diodes

The coinciding fields of view (FOV) of the different detector types can be exploited to calibrate the varying sensitivity of the AXUV diodes to the absolute measurements of the bolometer foils. This procedure assumes that there are no strong variations in plasma emission between adjacent FOV, allowing AXUV diode sensitivity calibrations to be calculated using regions between the full bolometer FOV. Consequently, this approach only offers a first-order calibration and that is sufficient as we only seek to obtain insights into the fast fluctuations in radiated power. Future work will aim to provide a complete cross calibration based on Bayesian inference techniques from bolometer inversions, and some preliminary results are already available in [36].

Only diodes with a similar FOV to the bolometers can be calibrated with this method. The overlap between two detector views is estimated from the goodness of

overlap, G , as

$$G = 1 - \int \int \frac{|\Omega(R, Z)^A - \Omega(R, Z)^B|}{\Omega(R, Z)^A + \Omega(R, Z)^B} dR dZ. \quad (1)$$

Here, $\Omega(R, Z)^A$ and $\Omega(R, Z)^B$ are the solid angles subtended by infinitesimal volumes centered on a point in the poloidal plane R, Z , normalised to each detector's etendue. The superscripts A and B represent the AXUV diodes and bolometers respectively. The quantity, G , represents the difference in geometric etendue integrated over the $R - Z$ plane, normalised to the combined etendue of both detectors. G was calculated by integrating equation 1 across a 240x240 R-Z grid, which included the tokamak wall geometry. G values of unity represent optimal mapping between the AXUV diode LOS and the bolometer LOS, and values of 0 indicate no overlap.

The calculated G values are presented in Figure 19 for each AXUV diode. Examples of the pairing between AXUV (red) and bolometry (blue) channels are indicated by the black regions in Figure 20. LOS with no match are evidenced by isolated red regions indicating AXUV diode FOVs with no bolometer FOV overlap, where these chords were excluded from the cross-calibration. If an LOS of any diode or bolometer malfunctioned during a discharge, that LOS was also excluded.

With this mapping, a calibration factor, $\alpha(t)$, for the voltage, $V_{AXUV}(t)$, measured by a given AXUV diode at a time t was determined from the average radiance measured by the corresponding foil bolometer, $\langle P_{bolo}(t) \rangle$. The calibration factor is then defined as $\alpha(t) = \langle P_{bolo} \rangle / \langle V_{AXUV} \rangle$ with the radiance measured by the AXUV diodes becoming $P_{AXUV}(t) = \alpha(t) V_{AXUV}(t)$. These were averaged over a nominal time period of $\Delta t_\alpha = 30ms$ to account for the relatively slower bolometer temporal response.

The most significant error in this calibration methodology is introduced by the assumption mentioned previously; the relative sensitivity of adjacent detectors is not greatly affected by any differences in viewing geometry. An upper bound for the uncertainty in the cross-calibration factor can therefore be estimated by considering the magnitude of any such difference in calibration factor, if the diode is calibrated with a bolometer with suboptimal mapping, i.e a detector pair with small G , instead of the line of sight with maximum overlap (G). The difference with this suboptimal mapping was computed as an average across the diverted plasma phase for all detector pairs and a 17.0% mean difference was obtained. This corresponds

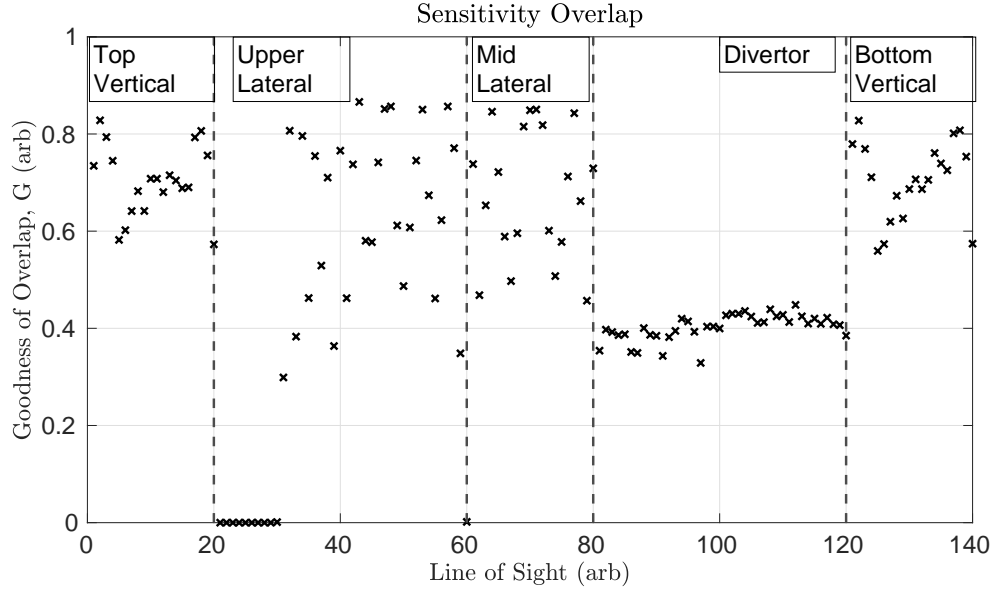


Figure 19. Goodness of overlap, G , as defined in equation 1 for the AXUV diodes with optimally mapped bolometers. High values mean good overlap between AXUV and adjacent bolometer FOVs and low values indicate bad overlap.

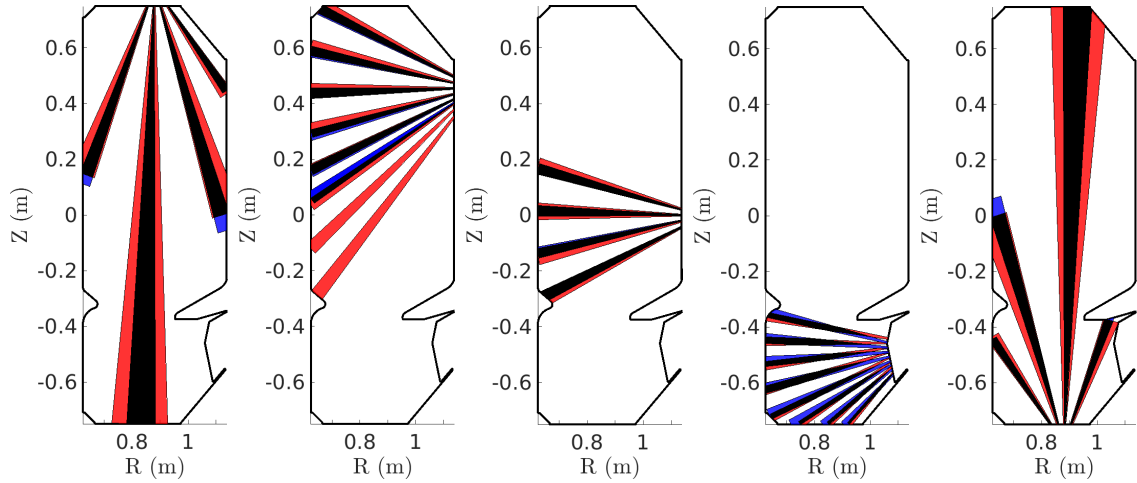


Figure 20. Examples of maximum overlap (black) between views of AXUV diodes (red) and foil bolometers (blue) for the top vertical, upper lateral, mid lateral, divertor and bottom vertical cameras (left to right).

to an estimated maximal cross-calibration uncertainty of $\sim 20\%$ when adding the contribution of the experimental spatial gradients in the plasma discharge.

The spatial variation in emissivity adds to the uncertainty of this approach that can be explored through the analysis of a baseline discharge. The selected plasma discharge (#70703) was a 280 kA, L-mode plasma with a diverted lower single null plasma phase. This discharge was selected as representative of typical plasma conditions for which this technique can be applied. The mean calibration factors calculated over an averaging period of 30 ms are presented in Figure 21, where the standard deviation indicates the uncertainty due to suboptimal mapping of a diode with adjacent bolometers. The large uncertainty in the calibration factor of LOS 127 is indicative of a large variation in plasma emission observed by adjacent detectors. This variation results from one detector observing the divertor leg and x-point, which are regions of high radiation emission, whilst the other is not. Furthermore, the difference between the calibration factors is increased due to the different spectral distribution of the divertor leg and x-point emission relative to the plasma core. The red-dashed lines in Figure 21 are overlaid to indicate the diodes that view the x-point where the calibration factor is peaked.

Figure 22 presents tomographic inversions of the bolometers, cross-calibrated AXUV diodes and uncalibrated AXUV diodes. Inversions with the uncalibrated diodes are not able to reproduce the expected emission at the x-point nor the divertor leg, as is obtained by the absolutely calibrated foil bolometers. Furthermore, large artefacts are apparent at the outer-wall and upper inner wall as the tomographic algorithm struggles to interpret the uncalibrated measurements. Conversely, considerably better agreement in emission location between the calibrated AXUV diodes and the bolometers is now obtained. This expected result shows the cross-calibration of the diodes relative to the bolometer foils has been implemented correctly.

This methodology was applied to a discharge (#70787) that features fast transient Edge Localised Modes (ELMs) that generate periodic bursts of radiation. Figure 23 left presents the radiated power inferred by the bolometers and cross-calibrated AXUV diodes over 100 ms of the discharge during which ELMs were present. The upper and lower bounds, depicted by the shadowed region, were calculated by computing inversions with the calibration factors modified by $\pm 20\%$ as justified previously. The difference in temporal response between the two systems is immediately apparent by the reduced sensitivity of the bolometers to the ELMs.

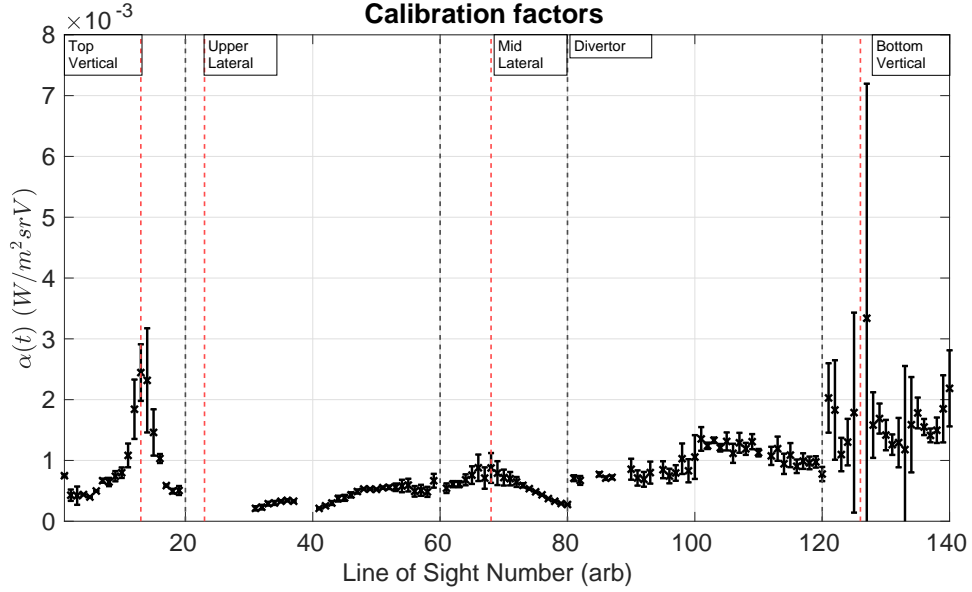


Figure 21. Calibration factors for discharge #70703 averaged over 30 ms for each AXUV diode LOS. Dashed black lines distinguish the five cameras whilst the red-dashed lines indicate diodes which view the x-point.

Figure 23 right presents the biggest ELM and the results indicate the radiated power during this ELM is at least double that of the inter-ELM period. This highlights the value and potential of cross-calibration when applied to fast radiation emission events whilst retaining a measurement of the absolute power level.

4.3. Grid Transmission Calibration on TCV

Determination of grid attenuation factors is required to infer the absolute radiated power during discharges with grids in place. The attenuation factors were estimated based upon pairs of ohmic plasma discharges with and without grids. A summary of the nominal plasma parameters of these discharges and the times used is provided in Table 4.3. The variation in the plasma emission between these pairs of repeat discharges is estimated to be below 10%. This estimate is based upon measurements of plasma density, temperature and emission using the Thomson Scattering, filtered photo-diodes and survey spectrometer diagnostics. The grid factors were calculated

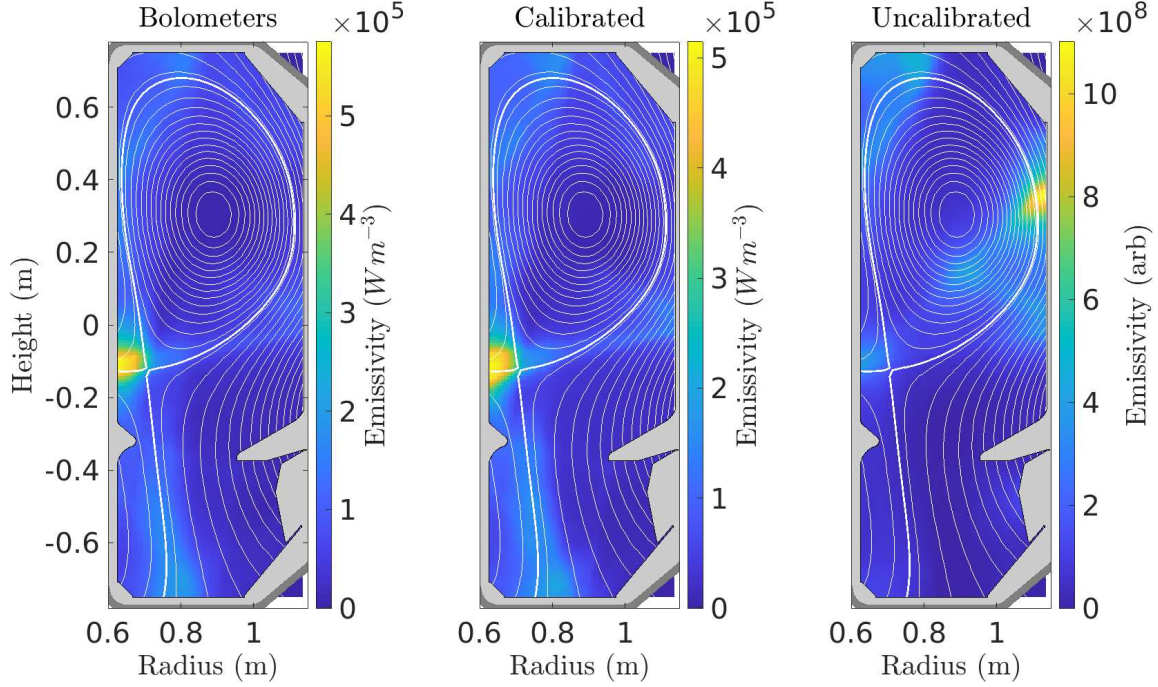


Figure 22. Emissivity across the poloidal cross-section as calculated by the bolometers (left), cross-calibrated AXUV photo-diodes (middle) and uncalibrated AXUV photo-diodes (right).

| Description | No grid | With grid | Time (s) | I_p (kA) | B_T (T) |
|--------------------|---------|-----------|-----------|------------|-----------|
| High Magnetic Axis | 75284 | 75285 | 0.20-1.80 | 250 | 1.43 |
| Diverted Plasma | 75263 | 75266 | 0.65-1.25 | 320 | 1.43 |

Table 4. Description of the pairs of discharges used in performing the grid calibration.

over a sampling period of 100 ms across the time range presented in Table 4.3. The optimal measurement of the grid attenuation requires a large signal and relatively stationary plasma conditions. For this reason, a threshold was placed on the signal strength and the variance in data during the averaging period.

Two plasma shapes were selected to sufficiently illuminate the maximum number of detectors. These were a high magnetic axis scenario, corresponding to a limited plasma that is vertically translated linearly in time over the range $z = -0.14 - 0.33m$,

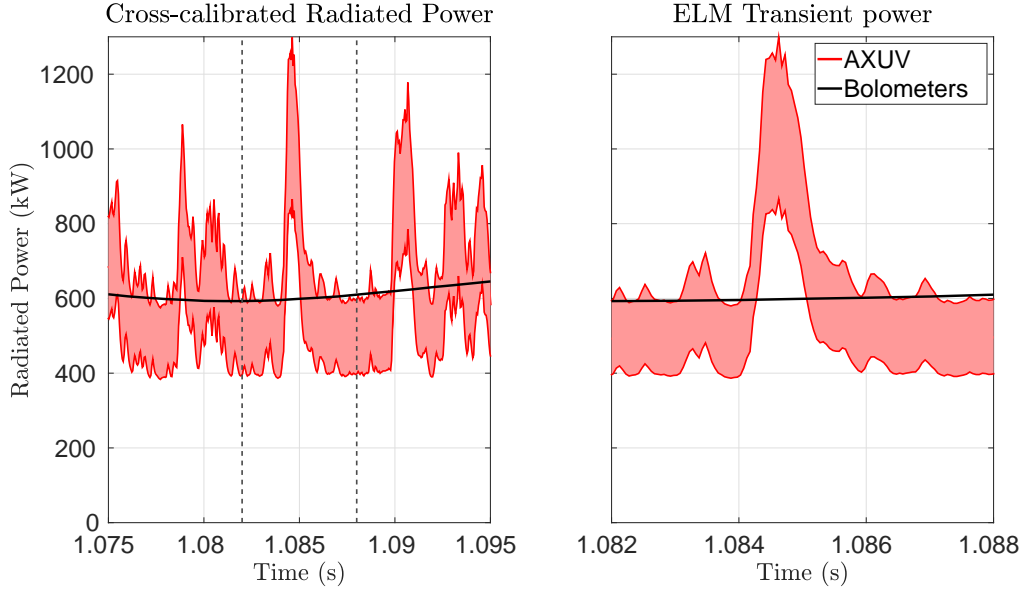


Figure 23. The radiated power of an ELM in kW as computed from tomographic inversions of the bolometers and cross-calibrated AXUV diodes. Left - time window of 20 ms with multiple ELMs. Right - 6 ms time window showing a single ELM.

and a diverted plasma configuration that illuminated the maximum number of detectors in the divertor camera. These discharges featured a density ramp, which led to a highly radiating configuration, and consequently, increased detector signal. The resulting factors are shown in Figure 24, where the black dashed lines indicate the design geometrical transparency factor of 0.53.

For the bolometers, the bulk of the calibration factors are found to lie close to the nominal transparency. Increases in the grid calibration factor are apparent at the edges of the upper lateral and bottom vertical camera, and this is attributed to geometrical misalignment of the rotating aperture wheel with respect to the detector. Realignment of the rotating aperture wheel is foreseen during an upcoming break in operation.

A larger variation in calibration factors is observed for the unfiltered AXUV diodes with an average of 0.60 ± 0.04 . Values higher than the geometrical transparency are presently attributed to reflections of visible light on the grid surfaces. Higher energy photons are expected to have significantly lower reflectivity and as the AXUV diodes are highly sensitive to visible light, this effect is strong.

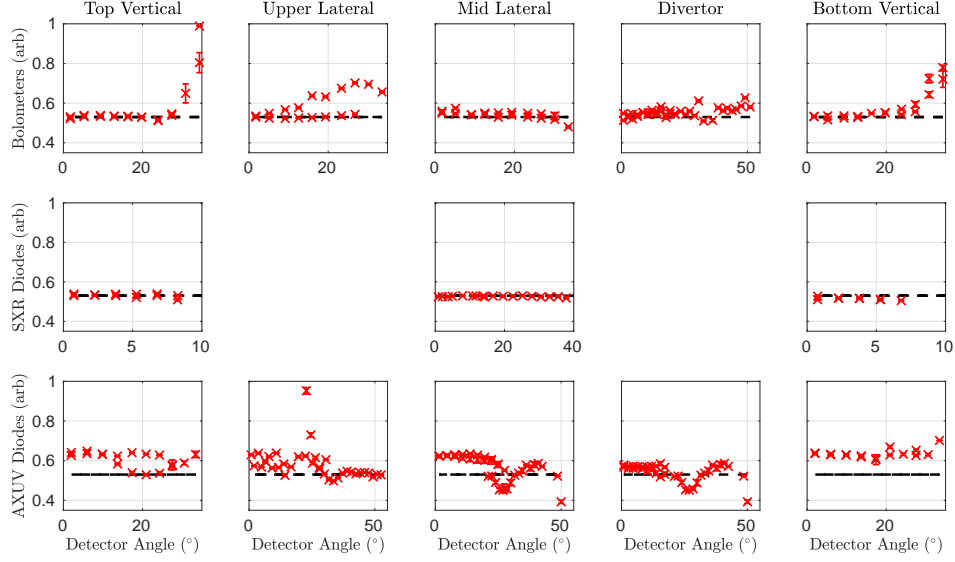


Figure 24. Grid calibration factors for bolometers, AXUV and SXR diodes. The geometrical transparency fraction of the grid (0.53) is superimposed by the black dashed line.

Based on the significant variation in calibration factors across several of the LOS, a separate calibration factor was adopted for each channel when grids were employed. It is challenging to accurately determine the effects of geometry and reflections during tokamak operation. For this reason, further laboratory measurements are planned to probe the cause of the higher than expected attenuation for the bolometers and the diodes.

The calibration factors computed for the SXR diodes were consistent across all channels and agreed well with the geometrical transparency fraction for all operational detectors with sufficient signal. This agreement relative to the AXUV and bolometer subsystems is attributed to the shorter wavelength of the high energy SXR radiation being less reflective and the small size of the aperture limiting the area of the grid illuminated. Edge effects from a potentially misaligned grid on the bottom vertical camera could not be assessed due to the low impinging radiance on the edge detectors. Based on these results, a global grid calibration factor of $f_{SXR} = 0.52 \pm 0.01$ was taken for all of the SXR cameras.

4.4. Bolometer Foil Performance

An Ohmic discharge with the magnetic equilibrium shown in Figure 25A was used in a performance comparison with the legacy system. A gas fuelling ramp, which increases the radiated power and changes the emission spectrum, was performed to provide a scenario to investigate the impact of the carbon coating. The ramp was initiated at 1.10 s until the plasma discharge disrupted at 1.58 s. An overview of the discharge parameters is presented in Figure 25F-I. Equivalent LOS between RADCAM bolometers and the legacy system were selected for comparison. The LOSs selected are indicated in Figure 25A where solid lines represent the legacy system and dashed lines the RADCAM. Multiple LOSs were averaged for each camera, except for the bottom vertical camera as the equivalent LOS in the legacy system was no longer functional.

The mid lateral camera measured significantly higher radiance relative to the legacy system over the entire discharge with the largest difference observed during plasma current ramp up and divertor formation (up to 0.4 s). During plasma current ramp up, the plasma is limited on TCV's inner carbon covered wall that liberates carbon impurities generating a strongly radiating cold plasma region close to the machine wall. The resulting emission is primarily carbon line emission in the ultraviolet to visible spectral range and increased foil absorption of these wavelengths with the carbon coating leads to the higher power measured.

The divertor LOSs observe the coldest part of the plasma, and there was an almost constant scaling factor in radiance between the two systems. There is a small relative increase in radiance during the early part of the density ramp, followed by a decrease as a cold plasma region forms at the machine floor and moves upwards towards the core and, finally, above the LOS. A similar observation is made by the bottom vertical camera. The camera's LOS includes a plasma-wall strike point close to the camera aperture that, again, generates strong carbon line emission and, consequently, a higher relative sensitivity. The difference in sensitivity diminishes towards the end of the discharge as the strong plasma radiation front detaches from the machine wall and the LOS's signal is again dominated by the plasma radiation from the hot core. This experiment was repeated with the strike point at several radial locations on the vessel floor to ensure the distance between the camera aperture and strike point did not generate systemic errors.

The radiances measured on the top vertical cameras, shown in Figure 25B, were

near identical between the two systems during the bulk of the discharge. Such a small relative difference between the two systems is surprising, given the larger differences on all other cameras. A manned inspection inside the tokamak revealed that a carbon tile was reducing the etendue of the entire camera in the toroidal plane. This tile has since been modified and re-installed to correct this, but unfortunately, a quantitative comparison with the legacy system is not possible for this camera.

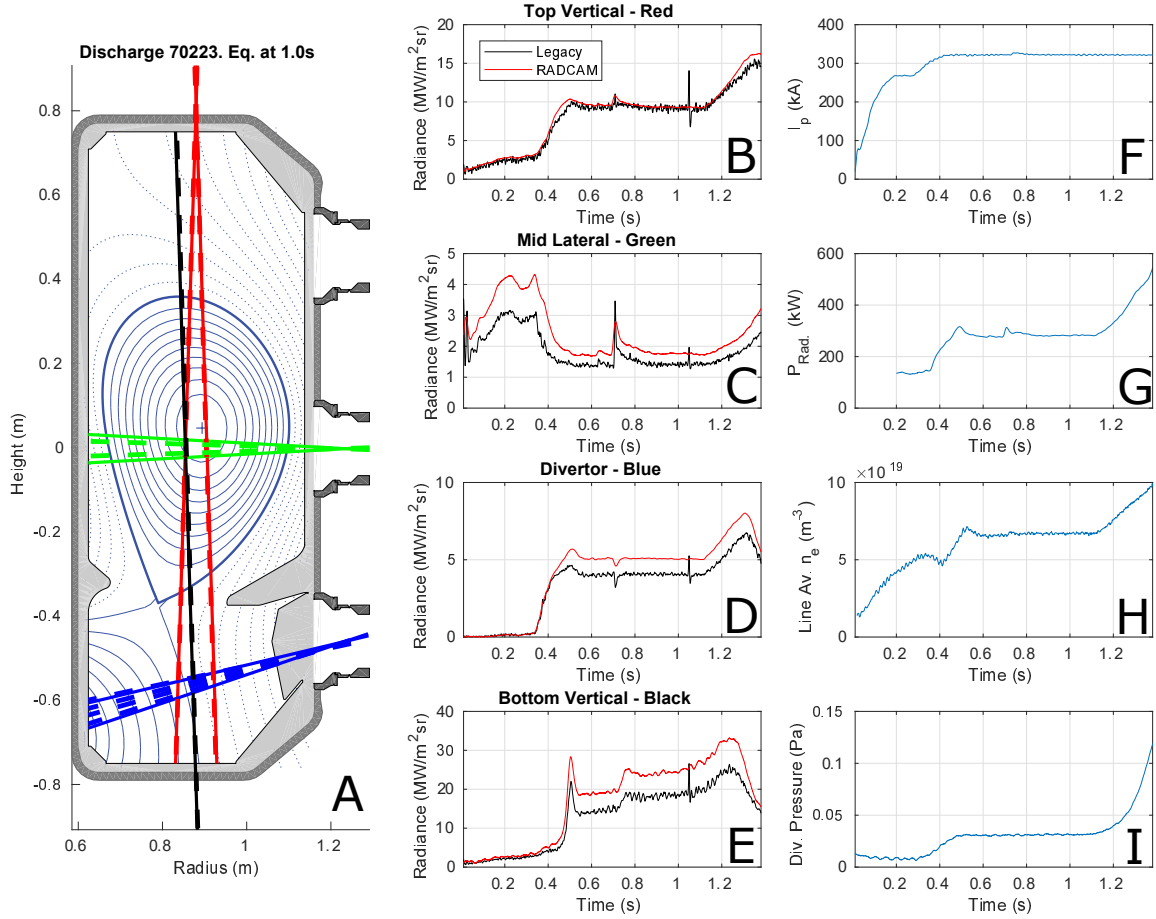


Figure 25. A - Magnetic equilibrium of a diverted Ohmic discharge overlaid with matching LOS for the RADCAM and legacy systems. The resulting signals on the top vertical (B), mid lateral (C), divertor (D) and bottom vertical (E) detectors. Global plasma discharge parameters presented in sub-Figures F-I.

The increase in measured radiated power for the carbon coated bolometer foil is apparent from all LOS except the top vertical camera due to the reduced

etendue. These results imply that radiated power in limited TCV discharges may have previously been underestimated by up to 35% and divertor emission by 25% for discharges similar to that presented. These values are significantly higher than those presented in Sheikh 2014[29] but are still within the possible differences in measured power based on gold and carbon reflectivity, previously presented in Figure 12. Specifically, the difference in absorbed power for photons below ~ 7 eV ranges between 20% and $\sim 450\%$, based on reflectivity. The signal to noise ratio improvement of the RADCAM system is also evident in all presented signals and was achieved without any significant reduction in temporal resolution by improved electronics and electrical component shielding.

4.5. Grid Resolution Study for Bolometer Inversions

An appropriate grid resolution for tomographically inverted images is required to balance inverted image quality, accuracy of radiated power inference and computational time. A grid resolution study was conducted using a SOLPS-ITER phantom with a known radiated power to study these outputs at different grid resolutions [20]. The SOLPS-ITER phantom was used merely to provide a baseline radiation emission pattern and not to study the physics involved in the discharge or the shape being simulated. The emission pattern was then used to create synthetic signals for the bolometers and those signal were in turn processed by the tomographic inversion algorithm, as described in Appendix 7.2. The resulting inverted images, produced for four grid resolutions, are presented in Figure 26

At a grid resolution of 15×35 pixels, inversion artefacts are apparent around the x-point and the structure is not well captured. Furthermore, significant radiation emission is incorrectly placed at the lower inner wall (bottom left). Increasing the grid resolution resulted in sharper imaging of the x-point and a strong suppression of the inversion artefacts. In particular, the emission between the inner strike point and the x-point is well captured and the incorrect emission in the lower inner wall is removed. Small ‘streaking’ artefacts still remain at the highest grid resolution and work on the inversion algorithms is continuing to address this.

The radiated power was underestimated relative to the phantom by 2-10% across the grid resolution range explored. No trend between grid resolution and total inferred radiated power was observed. This is attributed to the constant parameters

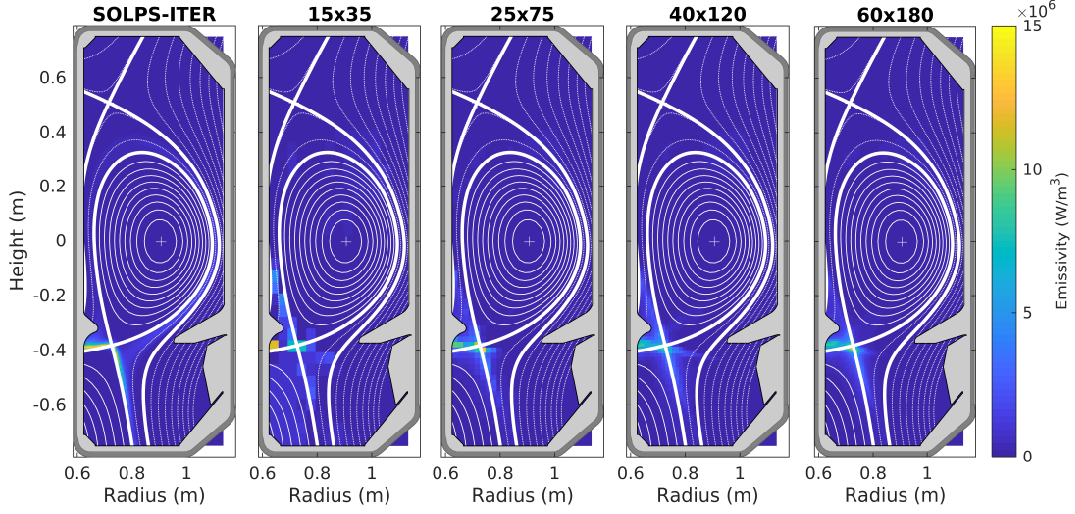


Figure 26. Tomographically inverted images of a SOLPS-ITER phantom (left) at different grid resolutions (indicted by sub-figure titles).

used for all the tomographic inversions, instead of optimised parameters for each grid resolution. This study demonstrates that the radiated power is a robust value (to within 10%) for all grid resolutions explored. The computational time of the inversions increased exponentially with grid resolution. An inversion was completed in ~ 10 s for a resolution of 25×75 pixels and just over 500s at 60×180 pixels on relatively modest computing hardware. Based on these studies, a grid resolution of 40×120 pixels was selected for automated inversions after each discharge to promptly provide accurate radiated power inferences and preliminary inverted images. A grid resolution of 60×180 pixels is currently foreseen for publications as it has produced the sharpest images with an acceptable processing time of less than 10 minutes.

4.6. Example Inversions of all Systems

Sample tomographic inversions for each system were conducted to demonstrate the tomographic capabilities of RADCAM. A lower single null Ohmic discharge during the un-baffled part of the campaign was chosen whose inversions are presented in Figure 27. This result demonstrates the full range of spatial information generated by RADCAM for total and SXR radiation. Firstly, the SXR radiation is seen to be centred on the high temperature core plasma, as expected. The bolometers identify

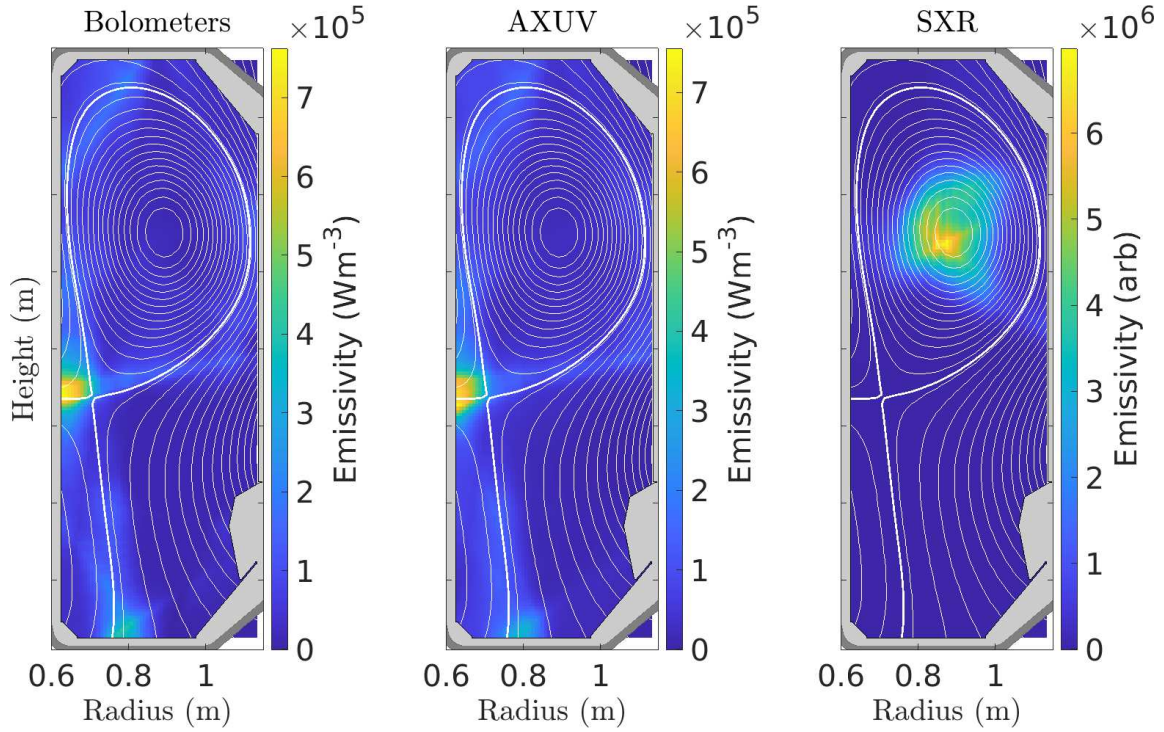


Figure 27. Example inversions of a L-mode Ohmic discharge for the bolometry (left), cross-calibrated AXUV (middle) and SXR filtered diodes (right).

the majority of the radiation as being emitted in the divertor region, close to the x-point. It is also possible to identify some strong emission at the outer divertor leg strike point and emission up the leg towards the x-point. Finally, the cross-calibrated AXUV diodes provide a similar result but with slightly smoother features. These inversions were not specially optimised and used a grid resolution of 60x180 pixels. The inversion methodology applied is described in Section 7.2. Optimisation of the tomographic inversion algorithm for this new system is outside the scope of this paper but is being explored elsewhere [36, 37].

5. Conclusions

A novel camera system incorporating bolometers, AXUV diodes and SXR filtered AXUV diodes has been designed, manufactured, installed and commissioned for use on the TCV tokamak. Design details regarding the thermal and electromagnetic

management of the three subsystems have been presented in this paper. Selectable grids to prevent stray ECRH power from entering the cameras are included, together with $\text{TiO}_2/\text{Al}_2\text{O}_3$ coatings inside the camera body to further absorb ECRH power that traverses the grids. The details for grid selection, qualification testing and calibration have been presented. A modular design was chosen to enable “plug and play” modifications of the LOS by exchanging subsystems as required. Through highly efficient use of valuable port space, RADCAM has liberated 16 vacuum vessel ports on TCV for other uses over the previous three separated systems.

The LOS of the bolometers and AXUV subsystems were optimised to cover the entire plasma vessel with some overlap designed between adjacent channels. The SXR subsystem FOV are denser in the plasma core, from which most SXR photon emission is expected. The cameras leverage shared LOSs so three types of detectors can be exploited in parallel. An example of this is the cross calibration of the AXUV diodes that suffer from sensitivity changes against the absolutely calibrated bolometers. This process allows AXUV diodes to provide calibrated radiation emission measurements at high temporal resolution through re-calibration. The technical details for this approach have been presented along with an example of its application over a fast transient ELM.

The foil bolometers were optimised for TCV by reducing their absorber thickness to $3\mu\text{m}$, reducing their thermal mass and increasing sensitivity. A 50 nm carbon coating was added to the absorber surface to reduce reflections for radiation below energies of 100 eV. Comparison of equivalent LOS between RADCAM and the legacy system showed an increase in measured radiated power of 25% in the divertor and up to 35% during the limited plasma start-up phase thanks to this addition. These values were higher than previously reported from TCV but remain well within the expected range based on gold reflectance.

An FPGA driven acquisition system has enabled automated calibrations prior to each plasma discharge pulse, allowing calibration stability studies and the availability of real time radiated power measurements. Such a study of the bolometer system showed that almost all detectors displayed a sensitivity and cooling time within 10% of the mean value. Foil calibration for 1000 discharges revealed that the mean system sensitivity varied by less than 2%, albeit with a few examples of up to 5%. The mean system sensitivity was found to be up to 3.5% lower at the start of daily operations before stabilising within 3 discharges. This variation was attributed to the foil temperature increases through calibrations, and the heat flux from plasma

emission, prior to reaching a more stable state for the following experiments.

Studies of image inversion resolution and inferred radiated power were conducted using a SOLPS-ITER phantom. The radiated power was found to be robust with less than 10% variation across a range of reconstruction grids. For routine analysis, a grid resolution of 25x75 pixels was selected for radiated power after every discharge. The computation time for this resolution was less than 10s on relatively modest computing hardware. Increasing the grid size resulted in significantly sharper resolution of the separatrix, emission around the x-point and removal of inversion artefacts. A grid resolution of 60x180 pixels is foreseen for scientific publications and can currently be computed in under 10 minutes on the same hardware. This approach has been reliably used on over 5000 discharges at the time of writing.

6. Acknowledgements

This work was supported in part by the Swiss National Science Foundation. This work has been carried out within the framework of the EUROfusion Consortium, funded by the European Union via the Euratom Research and Training Programme (Grant Agreement No 101052200 — EUROfusion). Views and opinions expressed are however those of the authors only and do not necessarily reflect those of the European Union or the European Commission. Neither the European Union nor the European Commission can be held responsible for them. The authors would like to thank Stefan Schmitt from the Fraunhofer Institute for Microtechnology and Microsystems for his role in developing the bolometer foil construction, Jean-Philippe Hogge for conducting the tests using the gyrotron stand, Frederic Dolizy for all his work related to the vacuum systems, testing and installation and Abha Sani for her contributions to the ECRH protection grid calibration.

7. Appendix

7.1. *Viewing Angles and Etendue*

The viewing angles for all systems were designed for maximum poloidal coverage whilst ensuring overlap between the LOS of adjacent detectors. The bolometers and AXUV arrays cover the entire plasma area and whereas the SXR system focussed on the hotter plasma core. Examples of adjacent viewing cones are shown in Figure 28

for all three systems. Solid lines indicate the region from where emission reaches the full detector and dashed lines the region where emission impinges only partially upon the detectors. The higher density of detector coverage in the divertor camera for the AXUV and bolometer systems provides higher resolution and ensures poloidal coverage without gaps. The poloidal aperture widths of the bolometer, AXUV and SXR slits were 4.0 mm, 1.0 mm and 1.5 mm respectively. Projections of the poloidal viewing cones of the top vertical, mid lateral and divertor cameras on the vessel floor and high field side (HFS) wall are presented in Figure 28, right.

The entrance slit widths of the toroidal plane were based upon the legacy system to guarantee sufficient detector irradiance with 20.0 mm, 2.0 mm and 10.0 mm for the bolometer, AXUV and SXR systems respectively. Even with the largest toroidal aperture size of 20.0 mm, the legacy bolometer system provided reliable tomographic inversions. The lateral SXR detectors are placed close to the apertures to increase their poloidal coverage and this results in a toroidal viewing projection that is larger than the bolometers at the HFS wall. This was deemed to still be suitable for tomographic inversions as SXR emission is only expected from the core of the plasma, where the toroidal viewing plane seen by the entire detector is 4.4 cm either side of the centerline at a radius of 0.9 m. Horizontal and vertical projections of the detectors in the toroidal plane are presented in Figure 29. Again, solid lines in the figure indicate the region with a full detector view and dashed lines indicate the region with a partial detector view.

7.2. Tomographic Inversion Methodology

The standard inversion code used at TCV relies on a minimum Fisher regularisation, where the spatial gradients are isotropic in the R and Z directions [21]. No knowledge of the magnetic equilibrium is provided to the inversion algorithm. Regions of negative emissivity are prohibited and the emissivity is related to the reconstructed chord signals by a transfer matrix that relies on a LOS approximation [38]. Further details on the additional tomography algorithms explored at TCV such as Tirkhanov Regularisation [21], neural networks [37], and Gaussian Processes [36] will be presented in subsequent papers.

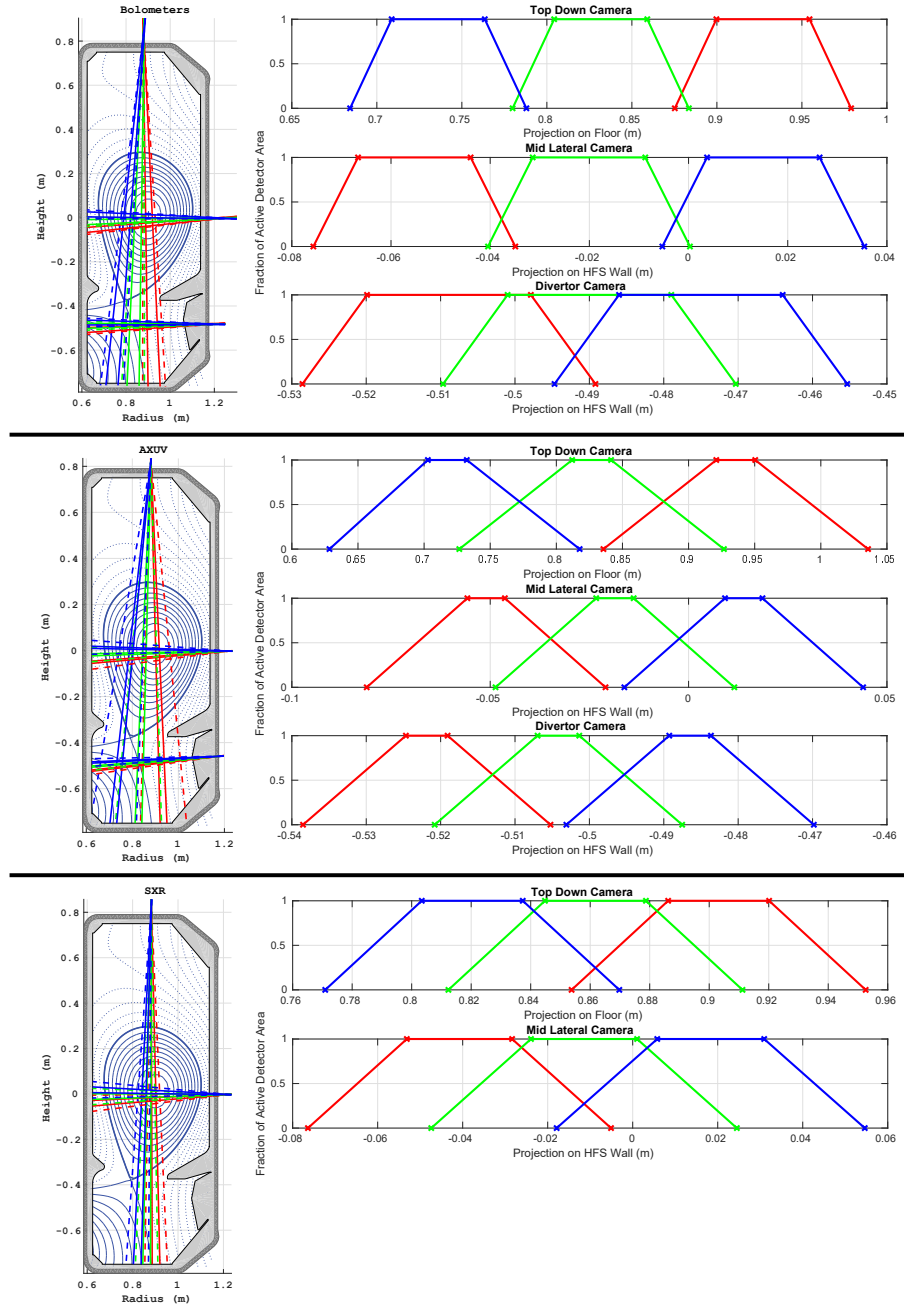


Figure 28. Poloidal viewing cones for three adjacent detectors in the upper, mid-lateral and divertor cameras of all three systems. Left - The solid lines superimposed on the magnetic equilibria indicate the region from which emission reaches the full detector and the dashed lines indicate the region where emission impinges partially on the detectors. Right - Projections of adjacent channels on the floor and HFS wall.

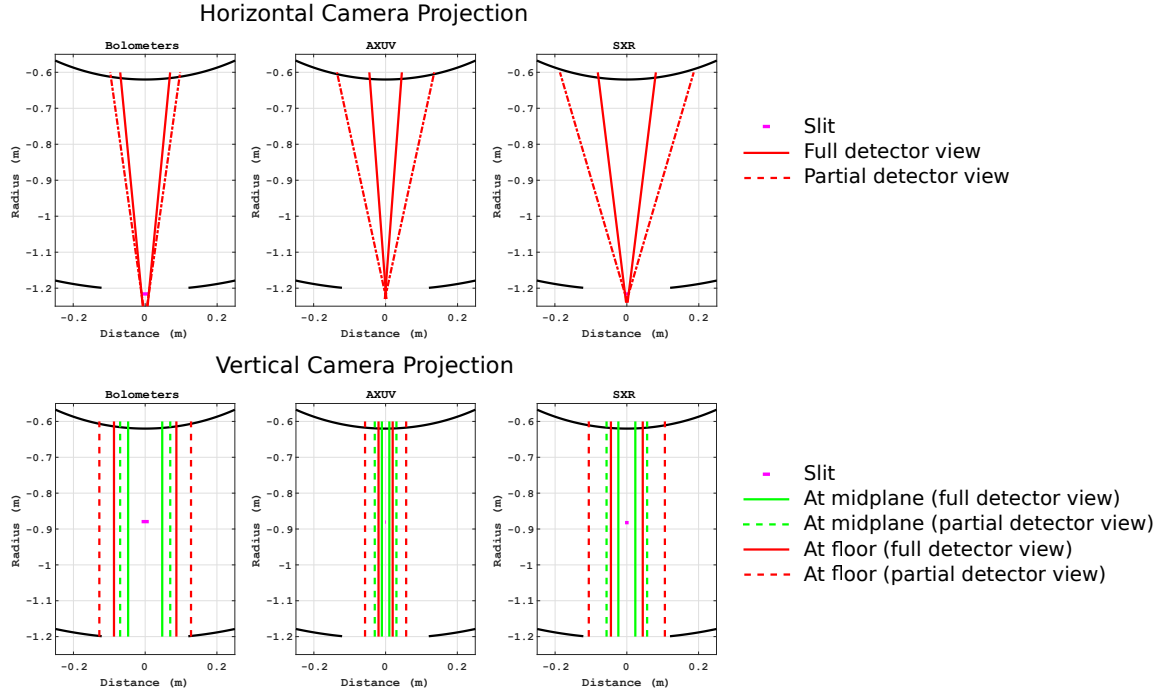


Figure 29. Toroidal view of the central detector of each mid-lateral camera (top) and projection of viewing angle of the vertical camera onto the vessel mid-plane and floor.

7.3. Bolometer Foil Calibration Stability

An automated calibration is performed before each TCV discharge, allowing stability analyses over time and information to debug potentially erroneous measurements obtained during experiments. The calibration outputs of cooling time and sensitivity for three representative foils over 1000 discharges are presented in Figure 30. These channels were selected as each is obtained by a different acquisition board. The cooling times were found to be extremely stable with less than 1.5% variation over the entire range. The sensitivity exhibited variations of less than 2%, when neglecting a few fluctuations of up to 5%. The timing and source of these fluctuation was explored but no trend has been determined to date.

The variation in mean system sensitivity and cooling time over an operational week is presented in Figure 31. A mean decrease of up to 3.5% in sensitivity was

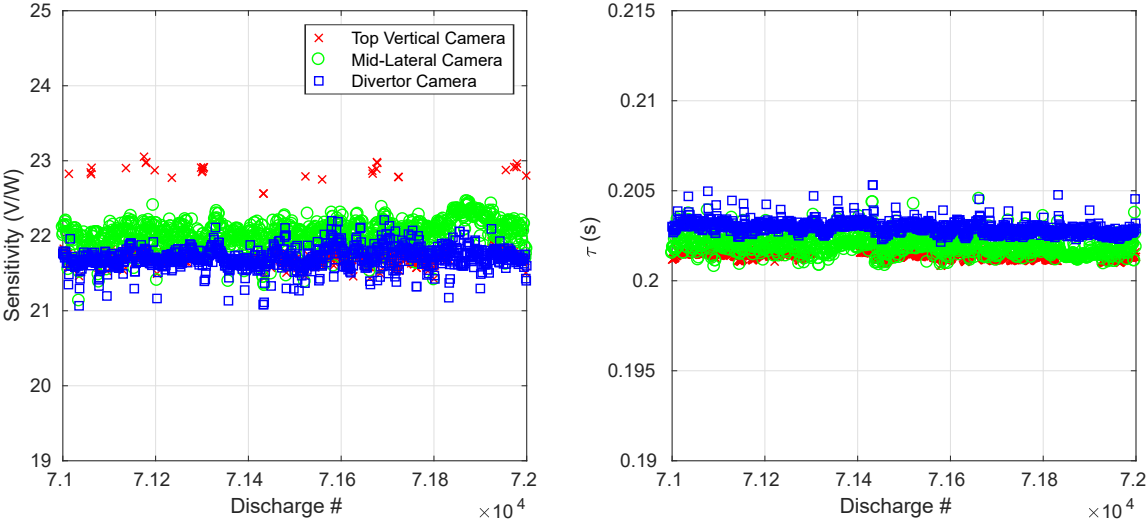


Figure 30. Sensitivity (left) and cooling time (right) for three representative channels in the top vertical, mid-lateral and divertor cameras calibrated prior to discharges 71000 to 72000.

observed at the start of each day that was generally resolved within 3 successive discharges. This “warm-up” in sensitivity is attributed to the temperature increase experienced by the foils as they undergo calibration and are irradiated during discharges. Once stabilised, the variation in sensitivity reduces to less than 1% for the remainder of the day. Likewise, the cooling time is up to 2.5% higher at the start of each day and once stable, it varies by than 1%.

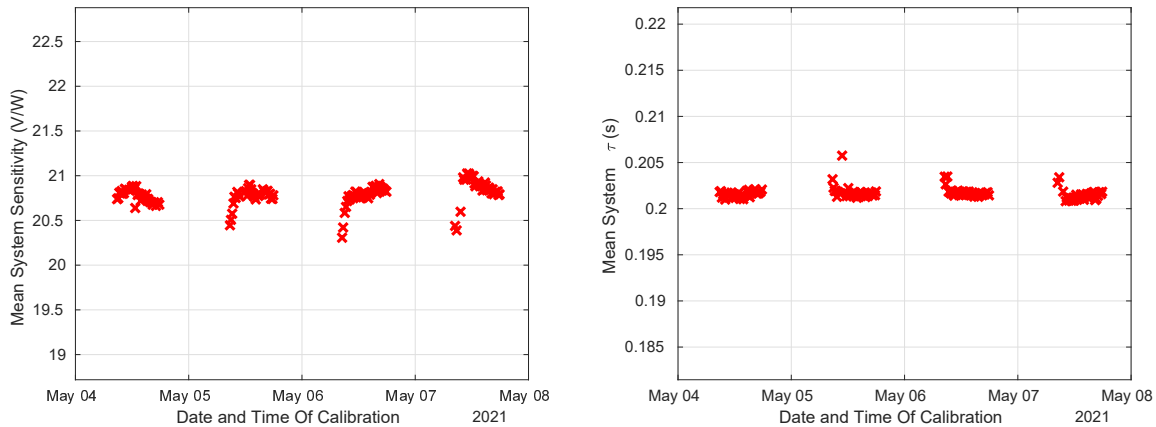


Figure 31. Mean sensitivity (left) and cooling time (right) of all foils over the course of an operational week.

8. Bibliography

- [1] Labit, B., et al. "Experimental studies of the snowflake divertor in TCV." *Nuclear Materials and Energy* 12 (2017): 1015-1019.
- [2] Harrison, J. R., et al. "Progress toward divertor detachment on TCV within H-mode operating parameters." *Plasma Physics and Controlled Fusion* 61.6 (2019): 065024.
- [3] Sheikh, U. A., et al. "Disruption mitigation efficiency and scaling with thermal energy fraction on ASDEX Upgrade." *Nuclear Fusion* 60.12 (2020): 126029.
- [4] Jachmich, S., et al. "Shattered pellet injection experiments at JET in support of the ITER disruption mitigation system design." *Nuclear Fusion* 62.2 (2021): 026012.
- [5] K. F. Mast, J. C. Vallet, C. Andelfinger, P. Betzler, H. Kraus, and G. Schramm, *Rev. Sci. Instrum.* **62**, 744 (1991).
- [6] H. Meister, T. Eich, N. Endstrasser, L. Giannone, M. Kannamüller, A. Kling, J. Koll, T. Trautmann, A. Team, P. Detemple, and S. Schmitt, *Rev. Sci. Instrum.* **81**, 10E132 (2010).
- [7] L. Giannone, D. Queen, F. Hellman, and J. C. Fuchs, *Plasma Phys. Controlled Fusion* **47**, 2123 (2005).
- [8] R. L. Boivin, J. A. Goetz, E. S. Marmar, J. E. Rice, and J. L. Terry, *Rev. Sci. Instrum.* **70**, 260 (1999).
- [9] M. L. Reinke and I. H. Hutchinson, *Rev. Sci. Instrum.* **79**, 10F306 (2008).
- [10] D. S. Gray, S. C. Luckhardt, L. Chousal, G. Gunner, A. G. Kellman, and D. G. Whyte, *Rev. Sci. Instrum.* **75**, 376 (2004).
- [11] M. Bernert, T. Eich, A. Burckhart, J. C. Fuchs, L. Giannone, A. Kallenbach, R. M. McDermott, B. Sieglin, and ASDEX Upgrade Team, *Rev. Sci. Instrum.* **85**, 033503 (2014).
- [12] Gao, X. "Diagnostics for first plasma study on EAST tokamak." *Physics Letters A* **372**.13 (2008): 2286-2290.
- [13] Zhang, X. L., et al. "Upgrade of absolute extreme ultraviolet diagnostic on J-TEXT." *Review*

- of Scientific Instruments **85.11** (2014): 11E420.
- [14] Lee, Seung Hun, et al. "Design and fabrication of a multi-purpose soft x-ray array diagnostic system for KSTAR." Review of Scientific Instruments **83.10** (2012): 10E512.
 - [15] Veres, G., Pitts, R. A., Wischmeier, M., Gulejova, B., Horacek, J. and Kalvin, S. (2007). Radiation distributions in TCV. Journal of nuclear materials, **363**, 1104-1109
 - [16] Degeling, A. W., et al. "AXUV bolometer and Lyman- α camera systems on the TCV tokamak." Review of scientific instruments **75.10** (2004): 4139-4141
 - [17] Furno, I., et al. "Fast bolometric measurements on the TCV tokamak." Review of Scientific Instruments **70.12** (1999): 4552-4556.
 - [18] Anton, M., et al. "X-ray tomography on the TCV tokamak." Plasma physics and controlled fusion **38.11** (1996): 1849.
 - [19] Reimerdes, H., et al. "Initial TCV operation with a baffled divertor." Nuclear Fusion **61.2** (2021): 024002.
 - [20] Wiesen, S., et al. "The new SOLPS-ITER code package." Journal of nuclear materials **463** (2015): 480-484.
 - [21] Kamleitner, J., (2015), "Suprathermal electron studies in Tokamak plasmas by means of diagnostic measurements and modeling". PhD Thesis, Ecole Polytechnique de Lausanne, Switzerland.
 - [22] Bernert, M., (2013), "Analysis of the H-mode density limit in the ASDEX Upgrade tokamak using bolometry." PhD Thesis, Max Planck Institute für Plasmaphysik, Germany.
 - [23] Floristán, M., et al. "Development and testing of 140 GHz absorber coatings for the water baffle of W7-X cryopumps." Fusion engineering and design **86.9-11** (2011): 1847-1850.
 - [24] D-TACQ Solutions Ltd, Blantyre, Glasgow. G72 0FB, Scotland UK, see <https://www.d-tacq.com/>
 - [25] Lovell, Jack, et al. "An FPGA-based bolometer for the MAST-U Super-X divertor." Review of Scientific Instruments **87.11** (2016): 11E721.
 - [26] Hagemann, H-J., W. Gudat, and C. Kunz. "Optical constants from the far infrared to the x-ray region: Mg, Al, Cu, Ag, Au, Bi, C, and Al₂O₃." JOSA **65.6** (1975): 742-744.
 - [27] Peterson, B. J., et al. "Bolometer diagnostics for one-and two-dimensional measurements of radiated power on the Large Helical Device." Plasma physics and controlled fusion **45.7** (2003): 1167.
 - [28] Schivell, J. "Performance of the Tokamak Fusion Test Reactor Bolometers." Review of Scientific Instruments **56.5** (1985): 972-974.
 - [29] Sheikh, U. A., et al. "A novel carbon coating technique for foil bolometers." Review of Scientific Instruments **87.11** (2016): 11D431.
 - [30] Schmitt, S., et al. "Radiation Resistant High-temperature Bolometer Sensors for Fusion Experiments." MikroSystemTechnik Congress 2021; Congress. VDE, 2021.
 - [31] Schmitt, S., 2010, "Hertsellung von langzeitstabilen Pt-Thermistoren mit hohen Temperaturkoeffizienten für anspruchsvolle Sensoranwendungen", Master's thesis, Institut für Mikrotechnik, Mainz, Germany.
 - [32] Garraud, A., Philippe C., and Alain G. "Thermal stability of Pt/Cr and Pt/Cr₂O₃ thin-film layers on a SiNx/Si substrate for thermal sensor applications." Thin Solid Films **540** (2013):

256-260.

- [33] Opto Diode Corporation, Camarillo, California, United States, see <https://optodiode.com/>
- [34] B.L. Henke, E.M. Gullikson, and J.C. Davis. X-ray interactions: photoabsorption, scattering, transmission, and reflection at $E=50\text{-}30000$ eV, $Z=1\text{-}92$, Atomic Data and Nuclear Data Tables Vol. **54** (no.2), 181-342 (July 1993).
- [35] Kramida, A., Ralchenko, Yu., Reader, J., and NIST ASD Team (2020). NIST Atomic Spectra Database (ver. 5.8), [Online]. Available: <https://physics.nist.gov/asd> [2021, October 28]. National Institute of Standards and Technology, Gaithersburg, MD. DOI: <https://doi.org/10.18434/T4W30F>
- [36] Moser, K., 2022, "Analyzing Fast Events via AXUV Diodes in the TCV Tokamak", Master's thesis, Ecole Polytechnique Federale de Lausanne, Switzerland.
- [37] Bossert, T., 2019, "Radiated power studies on TCV using neural networks", Master's thesis, Ecole Polytechnique Federale de Lausanne, Switzerland.
- [38] Jardin, A., 2017, "Soft X-ray measurements for impurity transport studies in tokamak plasmas", PhD thesis, Universite d'Aix-Marseille, France.